QUAID-E-AWAM UNIVERSITY RESEARCH JOURNAL

OF ENGINEERING, SCIENCE & TECHNOLOGY

MISSION STATEMENT OF QUEST

"To Provide quality and state-of-the-art education (coursework, practical training and research) in prescribed branches of Engineering and Science to the enrolled students in order to make them better professionals and better human beings; so that they become capable of contributing amicably towards national development".

Professor Dr. Saleem Raza Samo

Editor

Phone: +92-244-9370361 Fax: +92-244-9370362

E-Mail: srsamo@yahoo.com

FROM THE EDITOR'S DESK

Dear Researchers/Readers

Aslam-o-Alaikum

The editorial board thankfully acknowledges the support and cooperation of the individuals who have contributed in this issue. It is our highest priority to publish quality research papers in QUEST research journal. The undersigned is also thankful for very critical editing job being carried out by one of the young faculty member Mr. Mohammad Ramzan Luhur of Mechanical Engineering Department of this university.

The main purpose of our research journal is to provide a forum to researchers to highlight their related research work conducted in the universities / organizations of Pakistan. The contribution of authors will also motivate and compel the young researchers at national and international level to concentrate on the research activities in the universities and therefore must be encouraged.

Now a days it is noted, every where, with serious concern, that some people are badly involved in the act of plagiarism, which is very much condemnable. It is appreciated that the various universities of Pakistan have been reminded of HEC's strict rules and zero tolerance against plagiarism. In this regard the Higher Education Commission (HEC) has been taking necessary measure to stop such illegal activities. The universities seem to be serious for taking strict disciplinary action against acts of plagiarism such as resignation and dismissal of concerned faculty members. Therefore the editorial board of this research journal is also conscious and taking necessary action to off hook the Plagiarism.

It has been a continuous effort to search and bring the best research work carried out not only in QUEST, but also in other reputable national and international institutions. We hope you will find this issue quite informative and useful. Your valuable comments and suggestions for improvements are always welcome. May Allah give the power and strength to serve the humanity.

Prof. Dr Saleem Raza Samo

Editor-in-Chief

QURJEST

SYSTEM ANALYSIS OF MICROTURBINES AS AN OPTION FOR COMBINED CYCLE POWER GENERATION

Sunjay Velautham[*], Saleem Raza Samo[**] and Ahmed Hussain[*]

ABSTRACT

The demand for more efficient and lower emission power generation equipments has been increasing every year. The use of fossil fuels has produced emissions that are hazardous to humans and the environment. Due to technological advancements, a more efficient power generation equipment for distributed power generation has emerged. The microturbine produces power in the range of 25 – 500 kW and can run on a variety of fuels is gaining more acceptance in places such as hotels, supermarkets, hospitals and most importantly in industries and even oil rigs. However, the efficiency of the unrecuperated microturbine cycle which is still considered low is between 16- 20 % and for the recuperated cycle between 28 – 35 %. In order to make microturbines commercially viable, the efficiencies need to be equivalent with industrial gas turbines. This paper seeks to study these improvements by carrying out the parametric studies on the microturbine cycles for a combined cycle using water as the working fluid. The performance parameters such as the microturbine inlet temperatures and pressure ratios will be varied to compare and evaluate against various cycle configurations such as with and without recuperators. Finally a parametric comparison shall be carried out to determine the optimized cycle configurations and an optimized cycle will be proposed.

Keywords: environment, microturbine, optimised cycle, pressure ratio, recuperator

1. INTRODUCTION

In recent years, sustainability of energy has been a concern and a lot of research is being done by the global community. The introduction of higher efficiency microturbines has been seen as a alternative to limit the emissions of large power plants. Microturbines are generally used in distributed power generation. Distributed power generation is any small-scale power generation technology that provides electric power at a place closer to customers than a central generation station or plant [1]. As distributed power produces lesser power outputs, the size of the power generation equipments decreases, and therefore emissions are much easier to control. Various technologies are available for distributed generation, such as turbine generators, internal combustion engines, photovoltaic/solar panels, wind turbines, fuel cells and microturbines. This paper, analyses the outcomes of the microturbine technology that is available in the industry today.

The nominal power output of microturbines range from 25 kW – 500 kW [2]. The microturbine is a power generating turbomachine that is versatile in the utilization of fuels. This is because microturbines can run on various types of fuels, such as petrol, diesel , landfill gas, bio-fuels, ethanol and natural gas. For a country such as Malaysia which has agro based waste, such as POME, that is Palm Oil Methyl Ester obtained from the bio-degradation process, the bio-gas which is a sustainable fuel can be used in the microturbine. However, natural gas is currently used and it is the cleanest fossil fuel. Large power plants contribute to about 39 % of total CO_2 emissions, which is a greenhouse gas that causes global warming [3]. NO_x emissions from

*   Faculty of Mechanical Engineering, Universiti Teknologi Malaysia, Skudai ,Johor , Malaysia.
** Department of Energy & Environment Engineering, QUEST, Nawabshah, Sindh, Pakistan.

these power plants are also high that is around 50 part per million (ppm) as compared to the microturbine which produces around 9 ppm. Increasing the efficiency of the power generating equipments by 1 % reduces the CO_2 emissions by 2.5 %.

Table 1: Design Specifications for Micro turbine

Fuel	Natural Gas
Lower Heating Value (LHV)	55530 kJ/kg
Net Power Output	100 kW
Pressure Ratio	3 – 6
Turbine Inlet Temperature (TIT)	800°C–1000°C
Inlet Temperature (ambient)	30 °C
Microturbine and compressor blade diameter	0.15 m [8]
Isentropic efficiency of microturbine	0.83
Isentropic efficiency of compressor	0.84
Recuperator Effectiveness	0.7

Table 2: Design Specifications for Heat Recovery Steam Generator (HRSG)

Fuel	Unfired
Working Fluid	Water
HRSG Pressure	5 bar – 28 bar
Condenser pressure	0.05 bar
Inlet HRSG Temperature	390.21°C–747.9°C
Isentropic efficiency of Steam turbine	0.88
Pinch Point	20 °C
Stack Temperature	100 °C
Dryness Fraction	0.88

Large power plants contribute to about 39 % of total CO_2 emissions, which is a greenhouse gas that causes global warming [3]. NO_x emissions from these power plants are also high that is around 50 part per million (ppm) as compared to the microturbine which produces around 9 ppm. Increasing the efficiency of the power generating equipments by 1 % reduces the CO_2 emissions by 2.5 %.

2. SYSTEM CONFIGURATIONS

2.1 OPEN CYCLE UNRECUPERATED

In a open unrecuperated microturbine cycle as shown in Figure 1, air is induced into a compressor and then compressed to approximately 4 times its initial pressure. This air is then led into the combustion chamber where the mixture of compressed air and fuel is ignited. The exhaust gasses resulting from the combustion process is then let to expand in the microturbine before being disposed into the environment. The power obtained from the turbine runs the compressor and the generator. In a typical unrecuperated cycle, the efficiency is about 15%. [2]
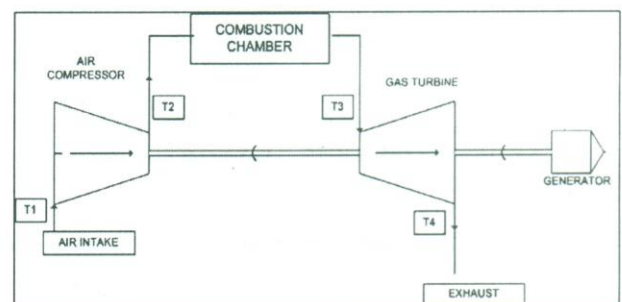

Figure 1: An unrecuperated cycle schematic diagram

2.2 OPEN CYCLE RECUPERATED

In a open recuperated cycle as shown in Figure 2, air is induced into a compressor and is then passed through a recuperator [7]. A recuperator enables heat exchange from the exhaust gasses from the turbine to the incoming air to the combustion chamber.
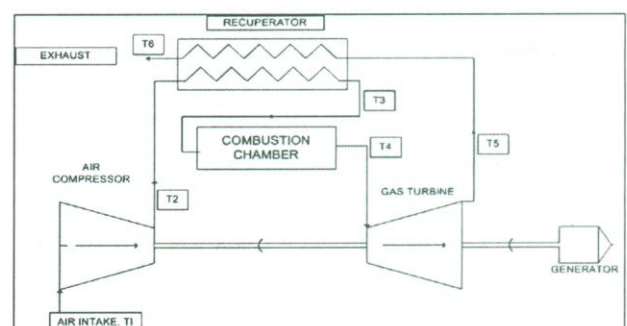

Figure 2: A recuperated cycle schematic diagram

This hot air enters the combustion chamber and the mixture of fuel and air is ignited. The exhaust gasses are let to expand in the microturbine. The exhaust gas from the microturbine passes through the recuperator before it is disposed to the environment. The efficiency of this system is said to be about 20 - 30%. [2]

2.3 COMBINED CYCLE POWER PLANTS

The combined-cycle unit combines the Rankine (steam turbine) and Brayton (gas turbine) thermodynamic cycles by using a HRSG to capture the energy in the gas turbine exhaust gases for steam production to supply a steam turbine as shown in Figure 3.

The efficiency of this combined cycle system can reach up to 60 % [2]. For a combined cycle using the exhaust from a recuperated cycle, the gas cycle is similar to that as shown in Figure 2 which is linked with the bottoming cycle as shown as the lower part in Figure 3.
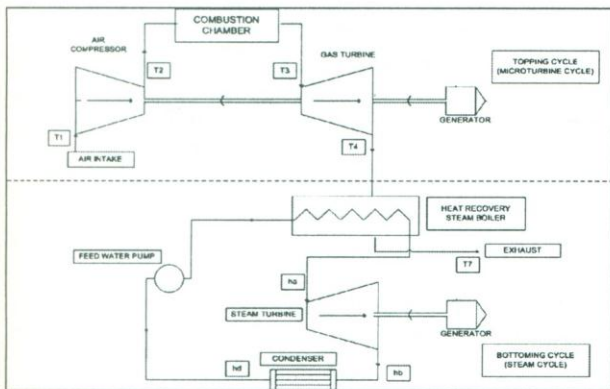

Figure 3: A combined cycle schematic diagram

3. METHODOLOGY

The sections details the formulas that are used to determine the efficiency of the unrecuperated (U), recuperated (R) and combined cycle unrecuperated (CCU) and recuperated (CCR). The design specifications used in these calculations are shown in Table 1 and 2.

3.1 CALCULATION OF PERFORMANCE PARAMETERS, MASS FLOW RATE AND ROTATIONAL SPEEDS FOR AN OPEN UNRECUPERATED CYCLE

The formulas laid out in this section are meant for the calculation of mass flow rate, rotational speeds, net work, the heat added to the cycle and thermal efficiency. In order to obtain the mass flow rate certain parameters such as the net power output, pressure ratio, compressor inlet temperature and turbine inlet temperature (TIT) must be assumed. The mass flow rate is then calculated from equation 1 that incorporates the isentropic efficiency of the microturbine, compressor, the specific heats and the T_2 and T_4 in terms of T_1 and T_3 respectively.

$$P_{net} = \dot{m}c_{pg}\left[T_3 - \left(T_3 - \eta_{microturbine}\left(T_3 - \frac{T_3}{\left(\frac{p_3}{p_4}\right)^{\frac{\gamma}{\gamma-1}}}\right)\right)\right] - \dot{m}c_{pa}\left[\frac{T_1\left(\frac{p_2}{p_1}\right)^{\frac{\gamma}{\gamma-1}} - T_1}{\eta_{compressor}}\right]$$

$$\rightarrow (1)$$

The total heat input into the system can be calculated by

$$Q_{input} = \dot{m}c_{pg}(T_3 - T_{2s}) \qquad \rightarrow (2)$$

The thermal efficiency for the unrecuperated system is therefore

$$\eta_{thermal} = \frac{P_T - P_C}{Q_{input}} \qquad \rightarrow (3)$$

To calculate the speed of the compressor or microturbine the blade and flow angles need to be set. The relation between the flow angle, α and the blade angle, β is given by

$$\beta_2 - \alpha_2 = incidence \qquad \rightarrow (4)$$

Where α = flow angle at impeller exit, β = blade angle at impeller exit [6]
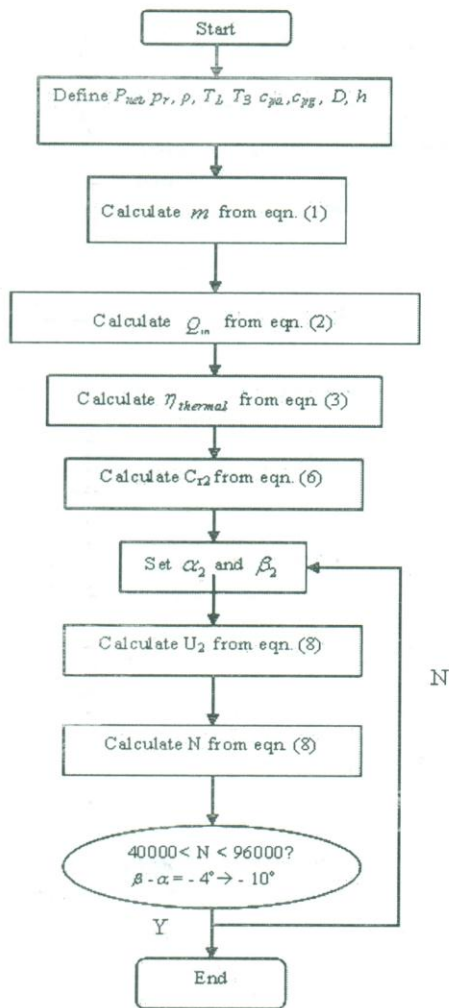
Figure 4: Performance parameters calculation flow for an unrecuperated cycle

The flow area for a centrifugal compressor or microturbine is

$$A = 2\pi rl \qquad \rightarrow (5)$$

From the mass flow rate and flow area, the absolute velocity in the radial direction for the gas flow can be calculated.

$$C_{r2} = \frac{\dot{m}}{\rho A} \qquad \rightarrow (6)$$

The blade tangential velocity, U_2 can be calculated from the relation below

$$U_2 = C_{x2} + W_{X2} \qquad \rightarrow (7)$$

The rotational speed, N can be calculated from

$$N = \frac{60 U_2}{\pi D} \qquad \rightarrow (8)$$

The steps and calculations can be summarized in the flowchart shown in Figure 4.

3.2 CALCULATION OF PERFORMANCE PARAMETERS, MASS FLOW RATE AND ROTATIONAL SPEEDS FOR AN OPEN RECUPERATED CYCLE

The method of calculation is same as the unrecuperated cycle except that before the mass flow rate is calculated, the thermal ratio (effectiveness) is set at 0.7 and the following equations are used,

$$\varepsilon = \frac{T_3 - T_{2s}}{T_5 - T_{2s}} \qquad \rightarrow (9)$$

$$c_{pg}(T_{5s} - T_6) = c_{pa}(T_3 - T_{2s}) \qquad \rightarrow (10)$$

3.3 COMBINED CYCLE ANALYSIS

After obtaining the mass flow rate from section 3.1 and section 3.2 for the unrecuperated cycle and recuperated cycle respectively, the combined cycle analysis to determine the power output from the steam turbine and combined cycle efficiency can now be carried on. The total heat transfer taking place from the turbine exhaust to the economizer in the HRSG can be calculated from the equations presented below. The condenser pressure (p_l) is set at 0.05 bar and the HRSG pressure (p_u) is varied from 15 to 34 bar. The isentropic efficiency of the steam turbine

is 0.88 and the dryness fraction is set to 0.88. The feedwater temperature to the HRSG, T_7 is set at 100 °C. Referring to Figure 5:
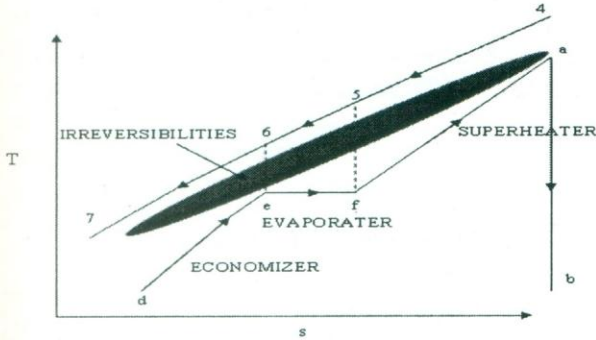
Figure 5: Temperatures and enthalpies in the gas and Rankine cycle

Where T_e is the saturated temperature at the desired pressure.

$$T_6 = T_e + PP \qquad \rightarrow (11)$$

PP here is the pinch point and is set at 20 ^{0}C. h_a and h_b can be calculated from the equation below

$$h_a = h \text{ at 20 bar when } s_a = s_b = x = 0.88 \text{ @ 0.05 bar} \quad \rightarrow (12)$$

$$h_b = h_a - 0.88(h_a - h_{bs}) \text{ and } h_{bs} = h \text{ @ 0.05 bar and } x = 0.88 \qquad \rightarrow (13)$$

The mass flow rate of steam can be calculated from the equation of balance as

$$\dot{m}_{gt} c_{pg}(T_4 - T_6) = \dot{m}_{st}(h_a - h_e) \qquad \rightarrow (14)$$

$$h_{fw} = h \text{ @ } T_7 \qquad \rightarrow (15a)$$

$$\dot{m}_{gt} c_{pg}(T_4 - T_{stack}) = \dot{m}_{st}(h_a - h_{fw}) \qquad \rightarrow (15b)$$

The temperature T_5 can now be calculated using the equation below

$$\dot{m}_{gt} c_{pg}(T_4 - T_5) = \dot{m}_{st}(h_a - h_f) \qquad \rightarrow (16)$$
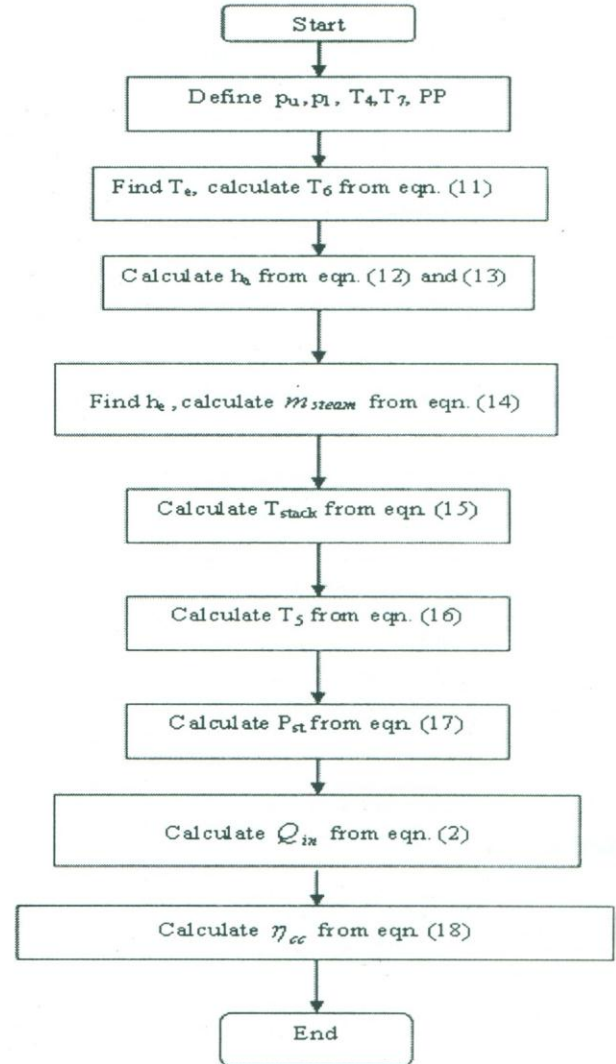
Figure 6: Calculation flow to obtain combined cycle efficiency

The power from the steam turbine can be calculated by

$$P_{st} = \dot{m}_{st}(h_a - h_b) \text{ where } h_b \text{ equals to h at 0.05 bar and } x = 0.88 \qquad \rightarrow (17)$$

The total heat input into the system can be calculated from equation 2. The combined cycle efficiency can finally be calculated

$$\eta_{cc} = \frac{P_{gt} + P_{st}}{Q_{in}} \qquad \rightarrow (18)$$

The same steps can be taken to determine the thermal efficiency for the recuperated cycle. The steps and calculations can be summarized in the flowchart shown in Figure 6.

4. RESULTS AND DISCUSSIONS

4.1 THE RELATION BETWEEN SPEED, ANGLE AND MASS FLOW RATE

Figure 7 shows the relation between the speeds of the compressor, microturbine and mass flow rate versus the blade angle, β. The single shaft compressor and microturbine must run at the same speed and the mass flow rate in the compressor and microturbine must be the same or else there will be a mismatch. However, the blade angles may be different. The graph is drawn for an incidence angle of -10 ° because it is the largest allowable value from the incidence angle relation. The graph shows that if the blade angle increases, the speed decreases for a constant mass flow rate. If the blade angle increases, the velocity triangle becomes smaller and the blade speed reduces. The flow angle α can be calculated from the incidence angle relation. The mass flow rates for the microturbine and compressor are the same for the same speeds but have different blade angles. As an example, the speed is set as 96000 rpm [2], which is an acceptable microturbine industrial speed. It can be seen from the graph that to maintain the speed and mass flow rate for the compressor and microturbine, the blade angles (α, β) are 13°, 23 ° and 7.8 °, 17.8 ° respectively for a constant mass flow rate of 0.61 kg/s.
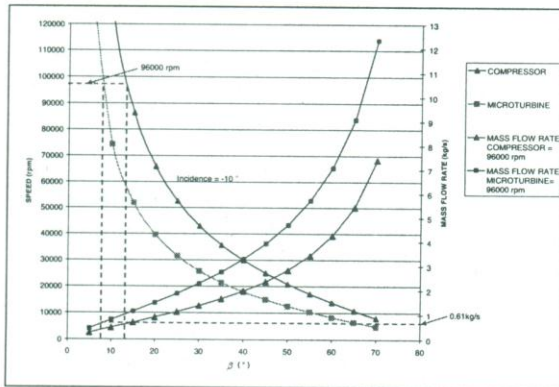
Figure 7: Compressor and microturbine speed vs blade angles

Taking into consideration the turbomachinery aspect, the angle β is taken as 60° and the incidence angle ia taken as of 10° . The compressor speed is matched to the turbine speed and by varying these angles, the best rotating speeds are shown in Table 3 .

Table 3: Compressor and microturbine speeds, blade and flow angles

Compressor Speed / rpm	96000
Microturbine Speed / rpm	96000
Compressor Angles (α / β)	13 / 23
Microturbine Angles (α / β)	7.8 / 17.8

4.2 THE EFFECTS OF PRESSURE RATIO ON EFFICIENCY

Figure 8 shows the efficiency of the unrecuperated and recuperated microturbine cycle at three values of TIT of 800 °C , 900 °C and 1000 °C and pressure ratio from a range of 3 to 6. It can be seen that the efficiency of the cycle increases as the pressure ratio and the TIT increases.
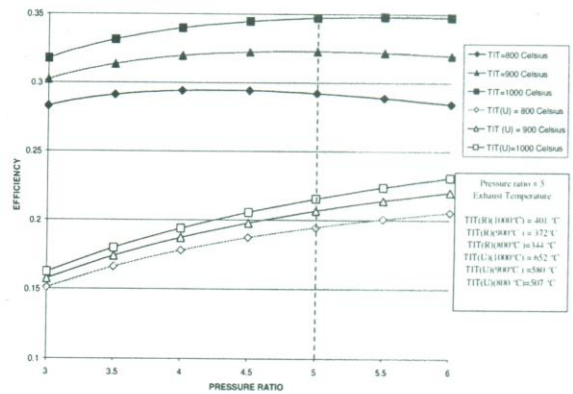
Figure 8: Efficiency versus pressure ratio. (Unrecuperated and Recuperated)

For an acceptable pressure ratio of 5 as shown in the above figure, it can be seen that for the unrecuperated cycle, the maximum efficiency obtained is 22 % that is for a TIT of 1000 °C. This is currently the highest limit of pressure ratio in the industry. From the graph it can be concluded that the

optimum efficiency for the unrecuperated cycle occurs at a much higher pressure ratio than 6. For the same pressure ratio and TIT, the recuperated cycle yields a higher efficiency that is almost 35 %. The values in the box shown in Figure 8 denote the exhaust temperatures for the indicated TIT's in Celsius. These exhaust temperatures are important parameters that are to be taken as the input temperatures to the HRSG for the combined cycle analysis.

4.3 THE EFFECTS OF PRESSURE RATIO ON UNRECUPERATED AND RECUPERATED COMBINED CYCLE EFFICIENCY

Figure 9 shows the efficiency of the combined cycle using the exhaust gas from the unrecuperated and recuperated Brayton cycle. The top three lines are for the recuperated combined cycle and the bottom three lines are for the unrecuperated combined cycle.
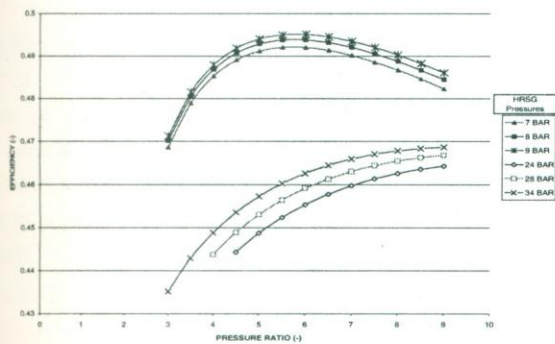
Figure 9: Efficiency unrecuperated combined and recuperated combined versus pressure ratio.

The TIT is set at 1000 °C and the pressure ratio of the microturbine is varied from 3 to 9. The total efficiency is calculated for 3 different HRSG working pressures of 24, 28 and 34 bar for the specified design specifications stated in Table 2. As afore mentioned, taking the microturbine pressure ratio of 5 it can be seen that the efficiency reaches around 46 % for a HRSG working pressure of 34 bar.

For the recuperated combined cycle, the TIT is again set at 1000 °C for the pressure ratio of 5. The HRSG working pressures is taken as 7,8 and 9 bar. It can be seen that the efficiency reaches around 50 % for a HRSG pressure of 9 bar. The cycle is not efficient at higher HRSG working pressures because of the irreversibilities (losses) that occur

in the shaded area as shown in Figure 4. There is a temperature cross over at higher HRSG pressures. A temperature cross over happens when the total heat supplied to the HRSG is lesser than the total heat required by the HRSG. The gas turbine exhaust cooling line clashes with the T-s line for the steam cycle. When the HRSG pressures exceed 34 bar for the unrecuperated combined cycle and 9 bar for the recuperated combined cycle, the total heat supplied to the HRSG is lower than the total heat required by the HRSG resulting in a temperature cross over.

5. CONCLUSION

From the various configurations and parametric analysis carried out in the preceeding sections, it can be concluded that the cycle that yields the best efficiency is the combined cycle using the exhaust from the recuperated Brayton cycle. It can also be seen that the required HRSG working pressures are much lower for the recuperated combined cycle as compared to the unrecuperated combined cycle. However, the specific power output obtained from the combined cycle using exhaust from the unrecuperated Brayton cycle is much higher compared to the earlier cycle. The total specific power obtained from the unrecuperated combined cycle at 34 bar is 414.87 kJ/kg gas and the total power obtained from the recuperated combined cycle at 9 bar is 231.64 kJ/kg gas. The cycle configuration for the best efficiency using the combined recuperated cycle is shown below in Table 4.

Figure 10: Efficiency unrecuperated, recuperated, unrecuperated combined and recuperated combined vs. pressure ratio

Table 4: Parameters for best efficiency cycle.

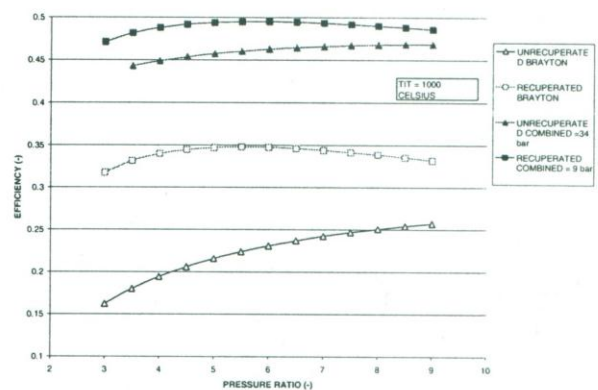| Parameters	CCR	CCUR
Pressure ratio	5	5
*T_1 (°C)	30	30
*T_2 (°C)	240.9	240.9
*T_3 (°C)	528.8	1000
*T_4 (°C)	1000	652.16
*T_5 (°C)	652.2	522.81
*T_6 (°C)	400.55	260.9
*T_7 (°C)	363.625	100
*T_8 (°C)	195.4	-
*T_9 (°C)	100	-
P_u (bar)	9	34
P_l (bar)	0.05	0.05
*h_a (kJ/kg)	3219	3672.7
*h_b (kJ/kg)	2384	2438.5
*h_e (kJ/kg)	743	1042
*h_f (kJ/kg)	2774	2803
*h_d (kJ/kg)	138.9	138
T_{sat} (°C)	175.4	240.9
PP (°C)	20	20
$\overset{\bullet}{m}_{st}$ (kg/s)	0.0506	0.0909
$\overset{\bullet}{m}_{gt}$ (kg/s)	0.5316	0.5316
T_{stack} (°C)	168.57	168.25
P_{st} (kW)	42.31	112.22
Q_{in} to Brayton cycle (kJ/kg)	541.92	873.02
η (%)	49.5	45.73
Q_{total} from Brayton (kW)	183.74	337.56
Q_{total} to Rankine (kW)	156.00	321.39

* Refer to Figures 2.3, 2.4, 2.5 and 3.6

REFERENCES

[1] Ackerman, T., Andersson, G., Sodder, L. 2001. Distributed Generation a Definition. *Electric Power Systems Research* 57, 195-204

[2] Traverso, A. and Massardo, A.F. 2005. Optimal design of compact recuperators for microturbine application. Applied Thermal Engineering 25: 2054-2071.

[3] Ho, J.C., Chua, K. J. and Chou, S.K. 2004. Performance study of a microturbine system for cogeneration application. *Renewable Energy* 29: 1121-1133.

[4] Yahya. S.M (2002). Turbines, Compressors and Fans. Second Edition. *Tata-McGraw-Hill,* India.

[5] Nag. P.K. 2002. Power Plant Engineering. Second Edition. *McGraw- Hill* International Edition. Singapore

[6] Sayers A.T. 1990. Hydraulic and Compressible Flow Turbomachines, *McGraw-Hill,* United Kingdom.

[7] McDonald, C.F. 2003. Recuperator considerations for future higher efficiency microturbines. *Applied Thermal Engineering* 23: 1463-1487.

[8] McDonald. C.F. 2000. Low-cost compact primary surface recuperator concept for microturbines *Applied Thermal Engineering* 20: 471-497.

NOMENCLATURE

η_{MT}	Brayton cycle efficiency
η_{CC}	Combined cycle efficiency
P_{MT}	Brayton cycle net power
P_{ST}	Steam turbine power
Q_{input}	Heat input to Brayton cycle
P_T	Microturbine power
P_C	Compressor power
$\overset{\bullet}{m}_{air}$	Mass flow rate of air
$\overset{\bullet}{m}_{st}$	Mass flow rate of steam
c_{pa}	Constant pressure specific heat of air = 1.005
c_{pg}	Constant pressure specific heat of gas = 1.15
γ_{air}	Specific Heat Ratio of air = 1.4
γ_{gas}	Specific Heat Ratio of Gas= 1.33
N	Rotational speed
r	Blade radius
l	Blade height
ρ	Density of air
D	Diameter of blade
α_2	Flow angle at impeller exit
β_2	Blade angle at impeller exit
p	Pressure
T	Temperature
ε	Thermal ratio for recuperator
h	Enthalpy

COMPUTING PARADIGM FOR IMPLEMENTATION OF VERY LARGE SCALE INTEGRATION (VLSI) IN COMPUTER ARITHMETIC

Sadaruddin Shaikh*

ABSTRACT

The computer arithmetic operations are to be processed in bulk when required by mobile phones, Wireless Application Protocol, coding / decoding and cryptography. The processor needs to be designed with hardware which should enable it for fast computing, low power consumption and low price. A computing paradigm supported by algorithm has been discussed in this paper. An implementation of Very Large Scale Integration hardware has also been described. The reduction in partial products reveals that the design has proved to give fast computation.

Index Terms: Computer Arithmetic, Algorithm, Computer Architecture.

1. INTRODUCTION

Historically, numerical values, counting and numbers are part of primitive civilization of human being. Through stone-age, people knew the techniques in different forms viz., marked bones, pebbles, clay tablets, colored balls and abacus etc. The computer arithmetic finds its major role in modern mathematical sciences. The decimal and binary number systems have revolutionized the computational methods.

Electronics emerged as a breakthrough field of science when semi conductor technology was developed to fabricate integrated circuits and further enhanced to very large scale integration. Millions of transistors can be etched to design multiple circuits on a square inch wafer. Nano-technology may take it to very intelligent research areas of further miniaturization.

Computing paradigm is the set of rules and methodology to formulate basic parameters and develop a sequence of systematic instructions or mathematical algorithm for a modified hardware and computer architecture.

Innovative research in computer arithmetic is useful in several applications such as: game theory, cryptography, coding/decoding, image/video processing, biometrics, graphics and animation and multimedia. The novel communication systems, wireless application protocol , cellular/mobile devices, personal digital assistant (PDA) with blue tooth and DoCoMo technologies and new gadgets require high speed computation at low consumption of power [1].

2. MODULAR MULTIPLICATION/DIVISION

Many algorithms have been proposed for computing modular multiplication/division using redundant number system or residue number system and performing high radix arithmetic [2].

A mixed radix (combination into one architecture) for VLSI implementation may reduce fabrication cost and lead to further miniaturization of the portable devices.

The operands are processed by two digits at each iteration. The algorithm has a linear array structure with a bit slice feature. The amount of hardware of an n-bit modular multiplier/divider is proportional to n. When the length of clock cycle is constant, and independent of n,

* Prof. Dr. Sadaruddin Shaikh is Dean Faculty of Technology, QUEST, Nawabshah, Sindh, Pakistan.

The n-bit modular multiplication = $[2/3 (n+2)]$ + clock cycles

The n-bit modular division= (2n+5 clock cycles)

The extended binary algorithm is an efficient way of calculating modular division. Consider the residue class field of integers with an odd prime modulus M. Let X and Y ($\neq 0$) be elements of the field. The algorithm calculates Z($<M$), where Z=X/Y(mod M). It performs modular division by inter-winning the procedure for finding the modular quotient with that for calculating (Y,M). The algorithm requires four variables, A,B,U,V. Variables A an B are initializes to Y and M respectively. A and B are integers and are allowed to be negative. ∂ represents α -β , where, α and β are values such that 2^α and 2^β indicate the upper bounds of |A| and |B| respectively, ρ represents min(α , β) and the condition, ρ =0 assures that A=0.

2.1 ALGORITHM FOR MODULAR DIVISION

Inputs: $M : ^{2n-1} < M < 2^n$, gcd (M,2)=1 and prime X,Y:0

X<M, 0<Y<M (gcd = binary algorithm)

Inputs: Z = X/Ymod M   Algorithm:

A:=Y; B:=M; U:=X; V:=0; ρ :=n; ∂:=0;

while $\rho \neq 0$ **do**

while A mod 2 = 0 **do**

A:=A/2; U:=U/2;mod M;

ρ := ρ -1; ∂ := ∂ -1;

endwhile

if <0 **then**

T:=A; A:=B; B:=T;

T:=U; U:=V; V:=T;

∂ :=- ∂;

endif

if (A+B) mod 4=0; **then** q:=1; **else** q:=-1;

A:=(A+qB)/4; U:=(U+qV)/4 mod M;

ρ:= ρ-1; ∂ := ∂ -1;

endwhile

if B=1 **then** Z:=V; **else** /* B=-1*/ Z:=M-V;

For calculating modular multiplication, consider the residue class ring of integers with an odd modulus M. Let X and Y be elements of the ring . The algorithm calculates Z($<M$),

where Z=XYR^{-1}(mod M), R is an arbitrary constant relatively prime to M and it usually takes the value of 2^n (radix-2) with an n-bit modulus M [3].

2.2 ALORITHM FOR MODULAR MULTIPLICATION

Inputs:

M :2^{n-1}<M<2^n and gcd (M,2)=1

X,Y : $0 \leq$ X,Y<M output: Z=$XY2^{-n}$ mod M

Algorithm:

A:=Y; U:=0; V:=X; ρ :=n;

while $\rho \neq$ 0 **do**

if A mod 2=0 **then** q:=0 **else** q:=1;

A:=(A-q)/2; U:=(U+qV)/2 mod M;

ρ := ρ -1;

endwhile

if U $\geq$ M **then** Z:=U-M **else** Z:=U;

In order to perform additions and subtractions without carry propagation, internal variables A,B,U and V as n-digit radix-2 signed digit numbers. It uses the digit set [1ˉ ,0,1], where 1ˉ denotes -1. An n-digit integer A = [a_{n-1}, a_{n-2}, ---, a_0], (a_i ε {1ˉ,0,1}) has the value $\Sigma^{n-1} a_i.2_i$.

For the interim sum h, carry digit c_i, it is required to find $s_i = h_i + c_{i-1}$ for each i without carry propagation. s_{ir} may be calculated to check the digits a_i , b_i and their preceding ones, a_{i-1}, b_{i-1}, and b_{i-2}. All digits of the result can be computed in parallel. The additive inverse is obtained by

changing the signs of all non-zero digits in it. Subtraction can be achieved by finding the additive inverse and performing addition.

In case of exponentiation, chained multiplications are required.

3. HARDWARE IMPLEMENTATION

The block diagram of simplified multiplier / divider is shown in figure 1. There are seven registers for storing A,B,P,D,U,M and V, selectors, a small control unit, and three adders, one of which is simpler. The controller is a combinational circuit [4]. It takes as inputs the least significant two digits of A,B,U, and V, the bit m1, the least significant three digits of P, as well as the bits d2 and d1, the flag 's', the two bits of the register state that stores the number of the step, and one bit of mode.
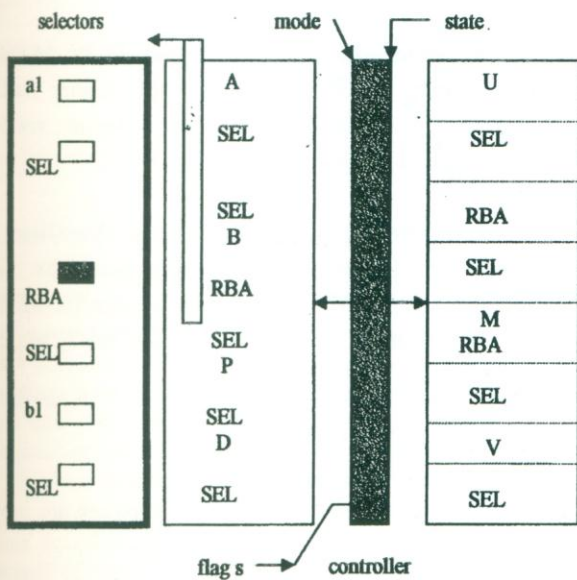
Figure 1: Block Diagram of Simplified Multiplier / Divider Circuit

The outputs of the controller are signals to all the selectors and the inputs to the flag 's' and the register state.

4. REDUCTION IN PARTIAL PRODUCTS (BINARY ARITHMETIC)

Binary multiplication is one of the most frequently used arithmetic operations in microprocessors. Implementation of binary multiplication is complex and multipliers are the largest and slowest non-memory blocks in contemporary microprocessors [5]. Therefore, it has a big impact on processor design and organization.

Targeting higher clock frequencies, deeper pipe line, demands low latencies with flexibility to be split in shorter stages. Low power consumption reduces cost.
A p*p bit product in simplest form is implemented by the generation of p partial products, each having **a** factored for $b[i]\,2^i A$ with partial product, the factor 2^i is realized by a hard wired shift of the multiplicand A, and the factor $b[i]\,\varepsilon\,\{0,1\}$, an individual bit in the binary representation of B, is employed by a partial product generator to select either $2^i A$ or zero as the ith partial product in the p-term sum. A series adder & an array adder may reduce the sum.

Reduced multipliers convert the binary operand B in to an alternative signed digit representation in a higher radix, allowing the generation of a much smaller number of partial products.

5. ELECTRON COUNTING ARITHMETIC

Addition and multiplication via a novel computation paradigm referred as ECA, electron counting arithmetic has been investigated in the past [6]. It is based on controlling the transport of discrete quantities of electrons within single electron tunneling circuit. Number of controllable electrons may not be higher than a given constant, determined by practical limitations.

The increase in processing power of arithmetic circuits has resulted due to modifications in the design and architecture of microelectronic circuits embedded in the microprocessor. A new circuit element for logic circuits viz., quantum tunnel junction is thought of as a 'leaky'

capacitor which can be controlled by the voltage across the junction. Charge transport through a tunnel junction can only occur in quantities of a single electron at a time.

A basic set of electron counting building blocks (more charge block), and periodic symmetric function block have to be developed. A thin layer of insulation separating two conductors works as an energy barrier, which inhibits charge transport under normal environment. The critical voltage can be calculated across the junction (which allows electron to flow / transport of charge i.e., tunneling).

Encoding integer values X directly as net extra charge is possible, hence arithmetic operations can be done directly in electron charges. Binary encoded n-bit operands are converted from digital to charge representation, add / subtract in charge format and convert back to binary digital representation.

6. CONCLUSION

The computer arithmetic operations are vital in mathematical sciences and require an algorithm supported by fast processor. The very large scale integration, IC chip circuitry has enabled to implement hardware for low cost and very fast computation of large data.

The computing paradigm consisting of systematic set of rules for the solution of arithmetic, including multiplication / division etc has been described. Algorithms developed in this regard have also been explained. The reduction of partial products, combination of architecture, and electron counting mechanism has proved that the implementation of the hardware gives fast computation at low consumption of power.

ACKNOWLEDGEMENT

REFERENCES

[1] M E Kaihara and N Takagi: "A hardware algorithm for modular multiplication / division." IEEE Transaction on computer, vol.54, no.1, pp.12, Jan'2005

[2] C K Koc, T A Car and B S Kaliski jr: "Analyzing and comparing M-multiplication algorithm." IEEE micro, vol.16, no.3, pp.26, June 1996

[3] P L Montegomery: "Modular multiplication without trial division." Math computation, vol.44, no.170, pp.519, April 1985

[4] M E Kaihara and N Takagi: "A VLSI algorithm for modular multiplication/division." Proc.16th symp, pp.220, June 2003

[5] P M Seidel, L D Mcfearin and D W Matula: "Secondary radix recordings for higher radix multipliers." IEEE Transcation on computer, vol.54, no.2, pp.111, February 2005

[6] S Cotofana, C Lageweg, and S Vassiliadis: "Addition related arithmetic operations via controlled transport of charge." IEEE Transaction on computer, vol.54, no.3, March 2005

THERMAL INSULATION OF ROOF USING HOLLOW CEMENT BLOCKS

Abdul Aziz Ansari[*], Mahmood Memon[**] and Noor Ahmed Memon[***]

ABSTRACT

Global warming is an international issue of the present era. The plains of our country Pakistan are tropical region where temperature soars even beyond 50 ^{0}C in summer causing a lot of discomfort and even deaths because of sun stoke during the months of scorching heat from May to August. As a matter of fact the major source of heat inside a building is the radiation through the roof which is directly exposed to sun shine; although same is true for walls, if they are also exposed to sun shine. However, the effect is more pronounced if relatively thin dividing walls rather than thick load bearing masonry walls are constructed. Hence ways and means must be adopted to resist this radiation. Attempts have been made by various researchers to keep the room temperature within tolerable limits with the help of different materials as insulators. However, the effectiveness of hollow blocks is not quantified so far. Therefore this study is aimed at finding the suitability of hollow blocks/sections as heat insulation. During this experimental study hollow blocks with different sizes were cast with OPC, white cement with marble dust and white cement with ceramics powder, because white materials reflect the heat more readily than absorbing it. Total twenty seven blocks were cast and tested. In some cases space in the hollow sections was filled with wood saw-dust. The results were encouraging. A minimum temperature difference of 11^{0}C was achieved in case of hollow space without wood chips, when top temperature was 53 ^{0}C and bottom temperature was 42 ^{0}C. Filling the hollow space with wood saw-dust showed significant effect on temperature difference which was observed to be as high as 15 ^{0}C.

1. INTRODUCTION

Now-a-days it is talk of era that global warming is increasing day by day because the average temperature of earth is increasing. Our country is tropical region where buildings need great capability to protect against day time heat and night chill. In the plains of this country the temperature some times exceeds 50 degrees Centigrade. It is very hard to survive in this situation without bringing down the temperature within tolerable limit. Every year many deaths are reported from various parts of Pakistan because of scorching heat during the months of May to August. Since last few years Nawabshah has remained the hottest place in Pakistan. The major source of heat inside the buildings is the heat radiation through the roof because of direct exposure to sun-shine. Therefore structure should be so designed that it is the most suitable for the climatic conditions of the region. For that many materials are in use to provide thermal insulation and also various techniques are in practice to provide heat resistance.

Basic to any discussion of thermal insulation and ventilation is an understanding of the way heat is transferred. Heat moves from place to place by conduction, convection, radiation or some combination of these modes whenever a temperature difference exists.

Besides the fact that great mass can store large quantities of heat even at low temperature e.g. thick masonry walls are slow to warm up in the heat of the day and slow to cool down during the night. A match is high temperature and little heat content. A large tank of water may have a low temperature but still have a large heat content.

* Associate Professor, Department of Civil Engineering, QUEST, Nawabshah, Sindh, Pakistan.
** Professor, Department of Civil Engineering, QUEST, Nawabshah, Sindh, Pakistan.
*** Assistant Professor, Department of Civil Engineering, QUEST, Nawabshah, Sindh, Pakistan.

The calculation of temperature within building of heating and cooling loads require knowledge of thermal conductivity, specific heat capacity and density of the materials of construction. The thermal resistance of air films adjacent to surfaces and of air spaces are also required and as the latter are dependent on the area of emission surfaces, data on these parameters are also needed. Thermal resistance is the quotient of thickness and thermal conductivity. The relationship between the thermal resistance and the thickness is most commonly assumed to be linear.

In our country the effect of solar radiation can be appreciable during some seasons and at certain times of the day. The orientation, design and materials used will all influence the amount of solar heat gain to which a building is subjected. A method of determining the degree and extent of solar gain has been developed which is called sol-air. This concept provides a solar increment to be added to the design air temperature used for horizontal roofs and facing walls. These increments range from 10 to 30 degrees centigrade. However, they apply for only a few hours per day and become of less significance if the building is designed to offset the effect of solar radiation. In area of high temperature rise during day and the night time temperature drops, the high solar-radiation effect is reduced to a minimum.

Several methods of insulation are in vogue. Rigid insulation can be employed as sheathing on the outside of wooden studs, as building board without plaster on the inside of the wood studs, and on the lower side of ceiling joists. It may be fixed as lath to receive plaster on the inner side of studs, and on the lower side of ceiling joists. It is nailed to furring strips, when used with masonry walls. Rigid insulation may be used on wooden and concrete roof decks under built up roofs.

While placing the insulation, precautions must be taken to protect the insulating materials from rain or other moisture by placing, at one time, only an area which can be covered in a short period, and never allowing the insulation un-protected over night.

It is good practice to insulate the effect of any leakage which may occur, and to provide a place where work can be stopped. It can be achieved by dividing the roof in to about 10 meters square with water cut-offs. These are provided by inserting a 40 cm strip being tightly cemented to the surface below the insulation and to the insulation itself.

Flexible insulation is provided in open spaces in the wall, ceiling, or roof construction where it will not be subjected to loads as it is easily compressible. Quilts or blankets are put between the studs and ceiling joists in frame construction between furring strips on masonry wall. Blanket insulation divides the space in to two or more air spaces. For greater efficiency, the insulation is fastened at the sides and ends so that there will be no air leakage between spaces.

Fill insulation is installed by pouring the loose granulated material into open spaces between the studs or between ceiling joists. The material may be blown into place through large flexible tubes employing low air pressure. Care is taken to insure the complete filling of space between studs.

Reflective insulation is fixed between studs, joists or rafter. It is held more tightly by using nailing strips. This type of insulation divides the space into two or more air spaces. It is essential that the insulation is fastened at the sides, top, bottom and all laps to restrict the air circulation between the two spaces.

A surface resists the transfer of heat according to its emissivity, its absorptivity and its reflectivity. At normal temperatures the emissivity and the absorptivity of a surface are the same, and the surface reflects what heat it does not absorb. The absorptivity of a surface for high temperature, i.e. solar radiation, may be quite different. This is important when insulating against sun's heat. Surface can lose heat by convection, so the resistance of outside surface is more a matter of climate, the temperature and speed of wind. The main effect of these factors on the resistance of a surface are therefore:

1. Cooling wind across an external surface will reduce its resistance.

2. The resistance of a corrugated surface is about 20% less than a plain surface of the same material because of its large area.

3. Surface of low emissivity, i.e. bright metallic surfaces, will have a high resistance, but this may be nullified if convection takes place as (1) above.

4. When a surface is radiating to an area of very low temperature, as to a clear sky in very cold, calm weather, the resistance of the surface can be decreased considerably.

5. The resistance of a horizontal surface will depend upon whether the transfer of heat is upwards or downwards, as convection will assist to take the heat away above and to keep it near the surface below.

The following are the major materials used for thermal insulation.

1. Fibre Glass.
2. Loose Fill.
3. Mineral Wool.
4. Plastic Fiber
5. Polyurethane Foams.
6. Phenolic Foam.
7. Cementitious Foam.
8. Nitrogen-Based Urea-Formaldehyde (UF) Foam.
9. Foaming Insulation Vehicles.
10. Structural insulating panels.
11. Insulating concrete forms (ICF).
12. Natural Fibers
13. Concrete Block Insulation.
14. Reflective type of insulation
15. Ceramics.
16. White Marble Dust.
17. Clay.
18. Wood Chips.
19. Ribbed (Hollow Blocks) Slabs.

20. Honey Comb Slab.
21. False Ceiling.
22. Hollow Baked Clay Blocks.
23. Hollow Blocks from Waste Materials.
24. Hollow Bricks.
25. Hollow Concrete Blocks.
26. Local Natural Materials such as; Straw, Shaving, Coffee Huts etc.

Light weight and hollow blocks are low cost items with adequate strength for building construction. It reduces dead load of structure. However, this is not very common in Pakistan.

A substantial work has already been done on various types of materials and techniques such as clay, ceramics, marble dust and wood chips etc. [1,2,3]. However, hollow blocks have not been tried in order to achieve thermal insulation. Main idea of using the hollow blocks is that the difference between outside temperature and inside temperature should be maximum. The room temperature should be reduced to such an extent that any need of air-conditioning or air coolers be avoided resulting energy savings which is so vital for a country like Pakistan where there is already acute shortage of electric power. This will have an over all favourable effect on the economy of the country. It may be mentioned here that Samo and others conducted study on prediction of the cooling energy requirement in buildings using the degree-days method [4,5].

This study is aimed to check the suitability of hollow sections to be employed as insulating medium with different materials. Wood chips were also filled in the hollow sections.

2. DEAILS OF PRESENT STUDY

This experimental study has been conducted mainly to study thermal insulation of various hollow blocks having different sizes of hollow sections and with different

materials. The major parameter of this study is to investigate the effectiveness of hollow space as thermal insulation and also its best suitable size. The other parameter is the type of material, while third parameter is the effect of wood chips filled in the hollow space on heat insulation. Twenty seven hollow blocks were cast and tested for heat insulation with and without wooden chips filled inside the hollow space.

The blocks were placed outside directly exposed to sunshine on stand specially manufactured for this purpose in order to have temperature measurements on the top and bottom of the blocks. The temperature measurements were recorded continuously from 9.00 A.M to 3.00 P.M. with time interval of one hour. Each test was conducted for three days. Electronic LCD type display system thermometer was used for these measurements. The complete details of the temperature measurements on the top and bottom of the blocks along with the difference are presented in table 1 to 6.

Table 1: Temperature Measurements of Cement Concrete Hollow Block

Type	Time hours	Hollow space 87.5mm x 87.5mm			Hollow space 81.25mm x 81.25mm			Hollow space 50mm x 50mm		
		Top °C	Bottom °C	Diff: °C	Top °C	Bottom °C	Diff: °C	Top °C	Bottom °C	Diff: °C
1st Day	11.00 A.M	38	33	5	38	33	5	38	32	6
	12 Noon	45	37	8	45	38	7	45	36	9
	1.00 P.M	47	38	9	47	38	9	47	39	8
	2.00 P.M	48	39	9	48	40	8	48	42	6
	3.00 P.M	48	39	9	48	40	8	48	42	6
2nd Day	11.00 A.M	43	38	5	43	38	5	43	38	5
	12 Noon	48	40	8	48	40	8	48	40	8
	1.00 P.M	48	41	7	49	41	8	49	42	7
	2.00 P.M	52	42	10	52	43	9	52	44	8
	3.00 P.M	53	42	11	53	44	9	53	45	8
3rd Day	11.00 A.M	39	33	6	39	33	6	39	33	6
	12 Noon	46	36	10	46	36	10	42	36	6
	1.00 P.M	48	40	8	48	39	9	46	40	6
	2.00 P.M	51	41	10	51	40	11	48	42	6
	3.00 P/M	52	41	11	52	41	11	51	43	8

Table 2: Temperature Measurements of White Cement With Marble-Dust Hollow Block

Type	Time hours	Hollow space 87.5mm x 87.5mm			Hollow space 81.25mm x 81.25mm			Hollow space 50mm x 50mm		
		Top °C	Bottom °C	Diff: °C	Top °C	Bottom °C	Diff: °C	Top °C	Bottom °C	Diff: °C
1st Day	11.00 A.M	36	31	5	36	33	3	36	33	3
	12 Noon	40	34	6	40	34	6	40	35	5
	1.00 P.M	43	37	6	43	36	7	43	36	7
	2.00 P.M	45	38	7	45	38	7	45	37	8
	3.00 P.M	45	38	7	45	38	7	45	38	7
2nd Day	11.00 A.M	41	37	4	41	37	4	41	36	5
	12 Noon	43	38	5	43	38	5	43	38	5
	1.00 P.M	46	39	7	46	39	7	46	39	7
	2.00 P.M	47	41	6	47	40	7	47	40	7
	3.00 P.M	47	41	6	47	41	6	47	40	7
3rd Day	11.00 A.M	37	33	4	37	33	4	37	33	4
	12 Noon	43	37	6	43	37	6	43	37	6
	1.00 P.M	44	39	5	44	38	6	44	38	6
	2.00 P.M	47	41	6	47	41	6	47	40	7
	3.00 P.M	46	40	6	46	40	6	46	40	6

Table 3: Temperature Measurements of White Cement With Ceramic Powder Hollow Block.

Type	Time hours	Hollow space 87.5mm x 87.5mm			Hollow space 81.25mm x 81.25mm			Hollow space 50mm x 50mm		
		Top °C	Bottom °C	Diff: °C	Top °C	Bottom °C	Diff: °C	Top °C	Bottom °C	Diff: °C
1st Day	11.00 A.M	36	33	3	36	33	3	36	33	3
	12 Noon	39	36	3	39	36	3	39	35	4
	1.00 P.M	42	39	3	42	38	4	42	38	4
	2.00 P.M	43	39	4	43	39	4	43	38	5
	3.00 P.M	44	39	5	44	39	5	44	39	5
2nd Day	11.00 A.M	41	37	4	41	37	4	41	36	5
	12 Noon	44	39	5	44	38	6	44	37	7
	1.00 P.M	45	39	6	45	39	6	45	39	6
	2.00 P.M	47	42	5	47	42	5	47	40	7
	3.00 P.M	47	42	5	47	43	4	47	40	7
3rd Day	11.00 A.M	37	33	4	37	33	4	37	33	4
	12 Noon	44	38	6	44	37	7	44	36	8
	1.00 P.M	45	39	6	45	39	6	45	38	7
	2.00 P.M	47	40	7	47	39	8	47	39	8
	3.00 P.M	47	41	6	47	39	8	47	39	8

Table 4: Temperature Measurements of Cement Concrete Hollow Blocks Filled With Wooden Chips.

Type	Time hours	Hollow space 87.5mm x 87.5mm			Hollow space 81.25mm x 81.25mm			Hollow space 50mm x 50mm		
		Top °C	Bottom °C	Diff: °C	Top °C	Bottom °C	Diff: °C	Top °C	Bottom °C	Diff: °C
1st Day	11.00 A.M	35	33	2	35	33	2	35	33	2
	12 Noon	43	35	8	43	34	9	43	34	9
	1.00 P.M	50	37	13	50	36	14	50	38	12
	2.00 P.M	53	38	15	53	38	15	53	39	14
	3.00 P.M	53	38	15	53	38	15	53	39	14
2nd Day	11.00 A.M	38	34	4	38	34	4	38	33	4
	12 Noon	43	36	7	43	35	8	43	35	8
	1.00 P.M	47	38	9	47	37	10	47	38	9
	2.00 P.M	49	39	10	49	38	11	49	39	10
	3.00 P.M	50	39	11	50	38	12	50	39	11
3rd Day	11.00 A M	37	33	4	37	33	4	37	33	4
	12 Noon	47	35	12	47	34	13	47	35	12
	1.00 P.M	49	36	13	49	35	14	49	38	11
	2.00 P.M	50	37	13	50	37	13	50	38	12
	3.00 P.M	51	37	14	51	38	13	51	39	12

Table 6: Temperature Measurements of White Cement With Ceramics Powder Hollow Blocks Filled With Wooden Chips.

Type	Time hours	Hollow space 87.5mm x 87.5mm			Hollow space 81.25mm x 81.25mm			Hollow space 50mm x 50mm		
		Top °C	Bottom °C	Diff: °C	Top °C	Bottom °C	Diff: °C	Top °C	Bottom °C	Diff: °C
1st Day	11.00 A.M	34	33	1	34	33	1	34	33	1
	12 Noon	42	34	8	42	33	9	42	34	8
	1.00 P.M	47	37	10	47	37	10	47	37	10
	2.00 P.M	49	38	11	49	38	11	49	38	11
	3.00 P.M	48	38	10	48	38	10	48	39	9
2nd Day	11.00 A.M	36	34	2	36	34	2	36	34	2
	12 Noon	42	35	7	42	35	7	42	36	6
	1.00 P.M	46	35	11	46	36	10	46	37	9
	2.00 P.M	47	37	10	47	38	9	47	37	10
	3.00 P.M	48	38	10	48	38	10	48	38	10
3rd Day	11.00 A.M	35	34	1	35	34	1	35	33	2
	12 Noon	42	35	7	42	34	8	42	35	7
	1.00 P.M	48	38	10	48	38	10	48	36	12
	2.00 P.M	49	39	10	49	39	10	49	38	11
	3.00 P.M	48	38	10	48	39	9	48	39	9

Table 5: Temperature Measurements of White Cement With Marble-Dust Hollow Block Filled With Wooden Chips

Type	Time hours	Hollow space 87.5mm x 87.5mm			Hollow space 81.25mm x 81.25mm			Hollow space 50mm x 50mm		
		Top °C	Bottom °C	Diff: °C	Top °C	Bottom °C	Diff: °C	Top °C	Bottom °C	Diff: °C
1st Day	11.00 A.M	35	33	2	35	33	2	35	33	2
	12 Noon	43	34	9	43	35	8	43	35	8
	1.00 P.M	46	37	9	46	36	10	46	37	9
	2.00 P.M	48	38	10	48	37	11	48	38	10
	3.00 P.M	47	39	8	47	37	10	47	37	10
2nd Day	11.00 A.M	36	34	2	36	34	2	36	34	2
	12 Noon	43	35	8	43	36	7	43	35	8
	1.00 P.M	46	36	10	46	37	9	46	36	10
	2.00 P.M	48	38	10	48	38	10	48	38	10
	3.00 P.M	48	38	10	48	38	10	48	39	9
3rd Day	11.00 A.M	35	33	2	35	33	2	35	33	2
	12 Noon	43	35	8	43	34	9	43	35	8
	1.00 P.M	47	38	9	47	37	10	47	38	9
	2.00 P.M	48	39	9	48	38	10	48	39	9
	3.00 P.M	47	38	9	47	38	9	47	39	8

3. RESULTS AND DISCUSSIONS

From these tables it can be observed that the maximum temperature occurs between 2.00 P.M. to 3.00 P.M, which soared upto 44 °C even in the month of April.

Table 1 presents the temperature measurements of concrete blocks observed for three days. It is apparent from this tables that temperature difference between top and bottom is more in concrete blocks with more hollow space and decreases with decrease in hollow space.
The maximum temperature difference observed is 11 °C in case of hollow space of 87.5 mm and 81.25 mm at the time of hottest atmospheric temperature.

Table 2 shows temperature measurement of blocks cast from white cement with marble dust. More or less it shows same trend of heat difference with respect to hollow space as it was in concrete blocks. However, the top of these blocks are becoming less hot as compared to

the concrete blocks, which was expected, because of white colour of the blocks. It can be observed from the table 2 that the temperature difference between top and bottom in this case is less than that observed in previous case. The maximum difference noted here is 7 degrees centigrade. Tables 3 presents the temperature measurements of white cement with ceramic powder hollow blocks. More or less its behaviour is identical to the case of marble dust blocks. Temperature observation for the hollow blocks filled with wooden chips is presented in tables 4 to 6. It is apparent from these tables that the maximum difference of 15 degrees centigrade can be achieved in case of cement blocks with higher value of hollow space while it decreases to 13 degrees in case of lowest value of hollow space. However, this difference is less in the cases of white cement with marble dust and ceramic powder, which is similar to the case of these blocks without wood chips.

The concrete blocks with wooden chips seem to be best possible technique. The blocks should be placed over the top of roof so that temperature difference at the top of roof of a room should be 15 degrees. It is expected that the temperature at the bottom of the roof inside the room would further decrease by a few degrees. Therefore the total temperature difference could be up to 20 degrees between outside and inside the room.

4. CONCLUSIONS

(i) Hollow blocks of concrete are more effective as thermal insulation in terms of temperature difference between up and bottom.

(ii) Hollow blocks of white cement with marble dust and ceramic powder are effective in terms of top temperature because of its white colour.

(iii) Temperature difference increases with increase in hollow space however, it is marginal, but in the case off white cement with marble dust and ceramic powder it is effect less.

(iv) A minimum temperature difference of 11 °C achieved in case of hollow space without wood chips. Where top temperature was 53 °C and bottom temperature was 42 °C. Filling of hollow space with wood chips has significant effect on temperature difference, which was observed as high as 15 °C.

REFERENCES

[1] Memon. M., Ansari. A. A. and Memon. A. B., "Effectiveness of Clay Tiles as Thermal Insulation", A Quarterly Journal of Science Technology and Development, Pakistan Council for Science and Technology, Islamabad, Volume No. 23, Number 2, April-June 2004, pp. 50-56.

[2] Memon. M., Ansari. A. A. and Memon. A. B., "Thermal Insulation of Roof Clay Tiles", Mehran University Research Journal of Engineering and Technology, Jamshoro, Volume 23, No. 3, July, 2004, pp. 183-190.

[3] Memon. M., Ansari. A. A. and Memon. A. B., "Experimental Study of Thermal Insulation Capability of Ceramics, Marble-Dust and Lime", Mehran University Research Journal of Engineering and Technology, Jamshoro, Volume 24, No. 2, April, 2005, pp. 105-114.

[4] Samo. S. R., Mari. H.B. and Saand. A., "Prediction of the Cooling Energy Requirement in Buildings Using the Degree-Days Method ", Mehran University Research Journal of Engineering and Technology, Jamshoro, Volume 19, No. 2, April, 2000, pp. 85-90.

[5] Samo. S. R., and Letherman. K. M., "An Energy Estimation method for Buildings in Pakistan", Mehran University Research Journal of Engineering and Technology, Jamshoro, Volume 18, No. 4, Oct: , 1999.

EXACT SOLUTIONS OF EQUATIONS OF STEADY PLANE MOTION OF AN INCOMPRESSIBLE FLUID OF VARIABLE VISCOSITY IN THE PRESENCE OF A TRANSVERSE MAGNETIC FIELD USING (r , ψ) – COORDINATES

Rana Khalid Naeem*, Waseem Ahmed Khan** and Rubina Faridi**

ABSTRACT

Exact solutions of the equations governing the motion of an incompressible fluid of variable viscosity in the presence of a transverse magnetic field are determined for the flows characterized by the stream function $\theta - f(r) = a\psi + b$, where θ and r are the polar coordinates.

Keywords: Exact Solutions, Steady Plane Flow, Fluid of variable viscosity, MFD flows.

1. INTRODUCTION

Martin's [1] introduced an excellent approach to study steady plane viscous flows. Martin's approach invloves using a natural curvilinear coordinate system (ϕ, ψ) in the physical plane (x, y), where ψ = constant are the streamlines and ϕ = constant is an arbitrary family of curves.

Naeem and Nadeem [2] extended Martin's approach to study steady plane flows of an incompressible fluid of variable viscosity, and determined same exact solutions to the flow equations. They also indicated that a large number of relations can be generated between viscosity μ and the temperature T using some of the solutions, and obtained empirical relations between μ and T suggested by Prandtl [3] and Poiseuille [4] on the basis of experimental results.

Labropulu and Chandna [5] have recently extended Martin's approach to study steady, plane viscous incompressible MHD aligned and non - MHD fluid flows, and determined some exact solutions when the polar representation of the streamlines patterns for these flows are of the form $[\theta - f (r)] [g (r)]^{-1}$ = constant by choosing the forms for the functions $f(r)$ and $g(r)$.

The objective of this paper is to determine same exact solutions of the equations governing the steady plane flows of an incompressible fluid of variable viscosity in the presence of a transverse magnetic field when the streamfunction ψ is characterized by

$$\theta - f(r) = a\psi + b \qquad \rightarrow (1.1)$$

where θ , r are the polar coordinates, and $a (\neq 0)$, b are arbitrary constants. To achieve our objective we, following Naeem and Nadeem [2] recast the fundamental equations of motion of the fluid under consideration in the presence of a transverse magnetic field in the Martin system (ϕ, ψ). By taking $\phi = r$, $x = r\cos\theta$ and $y = r\sin\theta$, we transform the flow equations into a new system of equations, and then determined exact solutions for various flows defined by equation (1.1).

2. FLOW EQUATIONS

The basic non–dimensional equations governing the motion of a finitely conducting incompressible fluid of variable viscosity in the presence of a transverse magnetic field are

---

* Department of Mathematics and Basic Sciences, NED University of Engineering and Technology, Karachi, Pakistan.
** Department of Mathematics, University of Karachi, Karachi, Pakistan.

$$u_x + v_y = 0 \qquad \rightarrow (2.1)$$

$$uu_x + vu_y = -P_x + \frac{1}{Re}\left[(2\mu\mu_x)_x + \{\mu(u_y + v_x)\}_y \right]$$
$$\rightarrow (2.2)$$

$$uv_x + vv_y = -P_y + \frac{1}{Re}\left[(2\mu\mu_y)_y + \{\mu(u_y + v_x)\}_x \right]$$
$$\rightarrow (2.3)$$

$$uH_x + vH_y = \frac{1}{R_\sigma}\left(H_{xx} + H_{yy} \right) \qquad \rightarrow (2.4)$$

$$uT_x + vT_y = \frac{1}{Re\,Pr}\left(T_{xx} + T_{yy} \right) + \frac{R_H E_C}{R\sigma}\left(H_x^{\,2} + H_y^{\,2} \right)$$
$$+ \frac{E_C \mu}{Re}\left[2\left(u_x^{\,2} + v_y^{\,2} \right) + \left(v_x + u_y \right)^2 \right]$$
$$\rightarrow (2.5)$$

where u, v are the velocity components , μ the viscosity of the fluid, H the z component of the magnetic field, T the temperature, Re the Reynolds number, R_H the magnetic pressure number, E_C the Eckert number, Pr the Prandtl number and $R\sigma$ the magnetic Reynold number. In equations (2.2) and (2.3) the function P is given by

$$P = p + R_H \frac{H^2}{2} \qquad \rightarrow (2.6)$$

where p is the pressure.

The equations (2.2) and (2.3) on introducing the vorticity function ω and the function L define by

$$\omega = v_x - u_y \qquad \rightarrow (2.7)$$

$$L = p + \frac{R_H H^2}{2} - \frac{\left(u^2 + v^2 \right)^2}{2} - 2\,\mu u_x \qquad \rightarrow (2.8)$$

becomes,

$$-u\omega = -L_x + \frac{1}{Re}\left[\mu(u_y + v_x) \right]_y \qquad \rightarrow (2.9)$$

$$v\omega = -L_y + \frac{1}{Re}\left[(4\mu v_y)_y + \{\mu(u_y + v_x)\}_x \right] \qquad \rightarrow (2.10)$$

Martin [1] introduced a curvilinear coordinates system in the (x , y)–plane through transformation equations

$$x = x(\phi,\psi) \qquad , \qquad y = y(\phi,\psi) \qquad \rightarrow (2.11)$$

where

$\psi(x, y)$ is the streamfunction and ϕ (x , y) = constant are arbitrary curves such that the Jacobian $J = \dfrac{\partial (x, y)}{\partial (\phi,\psi)}$ of the transformation is non–zero and finite. The first fundamental form in (ϕ,ψ) system is given by

$$ds^2 = E(\phi,\psi)\,d\phi^2 + 2F(\phi,\psi)\,d\phi d\psi + G(\phi,\psi)\,d\psi^2 \rightarrow (2.12)$$

where

$$E = x_\phi^{\,2} + y_\phi^{\,2}$$
$$F = x_\phi x_\psi + y_\phi y_\psi \qquad \rightarrow (2.13)$$
$$G = x_\psi^{\,2} + y_\psi^{\,2}$$

Differentiating equation (2.11) with respect to x and y and solving the resulting equations for $\psi_x, \psi_y, \phi_x, \phi_y$ yields

$$x_\phi = J\psi_y \quad , \qquad x_\psi = -J\phi_y$$
$$\qquad \rightarrow (2.14)$$
$$y_\phi = -J\psi_x \quad , \qquad y_\psi = J\phi_x$$

where

$$J = \pm\left(EG - F^2\right)^{\frac{1}{2}} = \pm\left(x_\phi y_\psi - y_\phi x_\psi\right) = \pm W \text{ (say } \rightarrow (2.15)$$

Let α be the angle between the tangent vector at the point (x , y) to the coordinate line ψ = constant and the x–axis , then

$$\tan \alpha = \frac{y_\phi}{x_\phi} \qquad \rightarrow (2.16)$$

Equation (2.14), utilizing equation (2.16) gives

$x_\phi = \sqrt{E}\cos\alpha , \quad x_\psi = \frac{1}{\sqrt{E}}\left(F\cos\alpha - J\sin\alpha\right)$
$\qquad\qquad\qquad\qquad\qquad\qquad\qquad \rightarrow (2.17)$

$y_\phi = \sqrt{E}\sin\alpha , \quad y_\psi = \frac{1}{\sqrt{E}}\left(F\sin\alpha + J\cos\alpha\right)$

The integrability conditions

$x_{\phi\psi} = x_{\psi\phi}$
$\qquad\qquad\qquad\qquad\qquad\qquad\qquad \rightarrow (2.18)$
$y_{\phi\psi} = y_{\psi\phi}$

for x and y , yield

$\alpha_\phi = \dfrac{J\,\Gamma_{11}^{\,2}}{E}$
$\qquad\qquad\qquad\qquad\qquad\qquad\qquad \rightarrow (2.19)$
$\alpha_\psi = \dfrac{J\,\Gamma_{12}^{\,2}}{E}$

where

$\Gamma_{11}^{\,2} = \dfrac{1}{2W^2}\left[-FE_\phi + 2EF_\phi - EE_\psi\right]$
$\qquad\qquad\qquad\qquad\qquad\qquad\qquad \rightarrow (2.20)$
$\Gamma_{12}^{\,2} = \dfrac{1}{2W^2}\left[EG_\phi - FE_\psi\right]$

The integrability condition for $\alpha(\phi,\psi)$, $\alpha_{\phi\psi} = \alpha_{\psi\phi}$, yields,

$K = \dfrac{1}{W}\left[\left(\dfrac{W\Gamma_{11}^{\,2}}{E}\right)_\psi - \left(\dfrac{W\Gamma_{12}^{\,2}}{E}\right)_\phi\right] = 0 \qquad \rightarrow (2.21)$

where K is called the Gaussian Curvature and equation (2.21) is called the Gauss equation. This equation represents a necessary and sufficient condition that E, F, G are coefficients of the first fundamental form in equation (2.12). We transform following Martin [1] and Naeem and Nadeem [2] , the equations (2.21), (2.4), (2.5), (2.7), (2.8), (2.9) and (2.10), into the (ϕ,ψ) system and we have the theorem.

Theorem: If the stream lines $\psi(x, y) =$ constant and the curves $\phi(x, y) =$ constant, left arbitrary, generate a curvilinear net in the physical frame, the equations governing the motion of an incompressible fluid of variable viscosity in the presence of a transverse magnetic field, is transformed into the following system

$q = \dfrac{\sqrt{E}}{W}$
$\qquad\qquad\qquad\qquad\qquad\qquad\qquad \rightarrow (2.22)$

$\omega J = -JL_\psi + \dfrac{A_\phi}{E}\left[2FJ\sin 2\alpha + \left(J^2 - F^2\right)\cos 2\alpha\right] + A_\psi$

$\left[F\cos 2\alpha - J\sin 2\alpha\right] + \dfrac{B_\phi}{E}\left[\left(F^2 - J^2\right)\sin\alpha\cos\alpha + JE\cos 2\alpha\right]$

$- B_\psi\left[F\sin\alpha\cos\alpha + J\cos^2\alpha\right]$
$\qquad\qquad\qquad\qquad\qquad\qquad\qquad \rightarrow (2.23)$

$- JL_\phi + A_\phi\left(J\sin 2\alpha - F\cos 2\alpha\right) + A_\psi E\cos 2\alpha - B_\psi E\sin\alpha\cos\alpha$
$\qquad\qquad + B_\phi\left(F\sin\alpha\cos\alpha - J\sin^2\alpha\right) = 0$
$\qquad\qquad\qquad\qquad\qquad\qquad\qquad \rightarrow (2.24)$

$\omega = \dfrac{1}{W}\left[\left(\dfrac{F}{W}\right)_\phi - \left(\dfrac{E}{W}\right)_\psi\right]$
$\qquad\qquad\qquad\qquad\qquad\qquad\qquad \rightarrow (2.25)$

$R_\sigma H_\phi = \left(\dfrac{GH_\phi - FH_\psi}{W}\right)_\phi + \left(\dfrac{-FH_\phi + EH_\psi}{W}\right)_\psi$
$\qquad\qquad\qquad\qquad\qquad\qquad\qquad \rightarrow (2.26)$

$\dfrac{T_\phi}{J} = \dfrac{1}{RePrJ}\left[\left(\dfrac{GT_\phi - FT_\psi}{W}\right)_\phi + \left(\dfrac{-FT_\phi + ET_\psi}{W}\right)_\psi\right]$

$\qquad + \dfrac{R_H E_C}{R_\sigma}\left[\dfrac{GH_\phi^{\,2}}{J^2} - \dfrac{2FH_\phi H\psi}{J^2} + \dfrac{EH_\psi^{\,2}}{J^2}\right]$
$\qquad\qquad\qquad\qquad\qquad\qquad\qquad \rightarrow (2.27)$

$\qquad + \dfrac{E_C Re}{4\mu}\left(4A^2 + B^2\right)$

$K = \dfrac{1}{W}\left[\left(\dfrac{W\Gamma_{11}^{\,2}}{E}\right)_\psi - \left(\dfrac{W\Gamma_{12}^{\,2}}{E}\right)_\phi\right]$
$\qquad\qquad\qquad\qquad\qquad\qquad\qquad \rightarrow (2.28)$

where ϕ and ψ are considered as independent variables. This is a system of seven equations in eight unknowns E , F , G , ω , L , μ , T and H of ϕ , ψ . In equations (2.23), (2.24) and (2.27), the functions A and B are given by

$$A = \frac{\mu}{J \, Re} \left[\begin{array}{l} \frac{q_\phi}{\sqrt{E}}\left(J \sin 2\alpha - F \cos 2\alpha\right) + q_\psi \sqrt{E} \cos 2\alpha \\ + \frac{q\alpha_\phi}{\sqrt{E}}\left(J \cos 2\alpha + F \sin 2\alpha\right) - q\sqrt{E}\,\alpha_\psi \sin 2\alpha \end{array} \right]$$

$$\to (2.29)$$

$$B = \frac{4\mu}{Re \, J}\left[\begin{array}{l} \left(F \sin \alpha + J \cos \alpha\right)\left(\frac{q_\phi \cos \alpha - q\alpha_\phi \sin \alpha}{\sqrt{E}}\right) \\ - \sqrt{E} \sin \alpha\left(q_\psi \cos \alpha - q\alpha_\psi \sin \alpha\right) \end{array} \right] \to (2.30)$$

The equation in the theorem form an underdetermined system since the coordinate lines ϕ = constant are left arbitrary. This underdetermined system can be made determinate in a number of different ways and one such possible way is to let $\phi(x,y) = r$, where (r, θ) – net is the polar coordinate system. Since we are interested in the flows characterized by $\theta - f(r) = a\psi + b$, we take $\phi = r$, $x = r\cos\theta$ and $y = r\sin\theta$ in the equation (2.13) and obtain

$$E = 1 + r^2 f'^2$$
$$F = r^2 f'a$$
$$\to (2.31)$$
$$G = r^2 a^2$$
$$J = W = r\,a$$

where

$$v = a\psi + b$$

The equations (2.22 – 2.30), using equation (2.31) becomes

$$q = \frac{1}{ra}\sqrt{1 + r^2 f'^2} \qquad \to (2.32)$$

$$\frac{\omega}{a} = -L_v + rA_r - rf'A_v - B_v \qquad \to (2.33)$$

$$-rL_r + r^2 f'A_r + (1 - r^2 f'^2)A_v - B_v rf' = 0 \qquad \to (2.34)$$

$$\omega = \frac{1}{a}\left[\frac{f'}{r} + f'' \right] \qquad \to (2.35)$$

$$R_\sigma H_r = \left(\frac{GH_r - aF\,H_v}{ar}\right)_r + a\left(\frac{-FH_r + aEH_v}{ar}\right)_v \qquad \to (2.36)$$

$$T_r = \frac{1}{Re\,Pr}\left[\left(r\,aT_r - r\,a\,f'T_v\right)_r + a\left(-r\,f'T_r + \frac{(1 + r^2 f'^2)T_v}{r}\right)_v \right]$$
$$+ \frac{R_H E_C}{R_\sigma a\,r}\left[a^2 r^2 H_r^2 - 2a^2 r^2 f'H_r H_v + a^2(1 + r^2 f'^2)H_v^2\right]$$
$$+ \frac{E_C\mu}{Re}\left[\frac{(rf'' - f')^2}{a\,r} + \frac{4}{a\,r^3}\right]$$

$$\to (2.37)$$

where

$$A = \frac{\mu}{a\,r\,Re}(rf'' - f') \qquad \to (2.38)$$
$$B = -\frac{4\mu}{a\,r^2\,Re}$$

and E, F, G are given by equation (2.31). We note that the Gauss' equation (2.28) is identically satisfied

3. SOLUTIONS

In this section, we determine the solutions of equations (2.32–2.37) for various flows.

(I) For the flows with $\theta - A_1 r$ = constant as streamlines, we have

$$f(r) = A_1 r \qquad \to (3.1)$$

Equations(2.32–2.37), utilizing equation (3.1) become

$$q = \sqrt{\frac{1 + r^2 A_1^2}{a\,r}} \qquad \to (3.2)$$

$$L_r = \frac{r}{4}A_1^2 B + \frac{r^2}{4}A_1^2 B_r + \left(-\frac{3A_1}{4} - r^2 A_1^3\right)B_v \to (3.3)$$

$$L_v = -\frac{A_1}{a^2 r} + \frac{A_1 rB}{4} + \frac{A_1 r^2 B_r}{4} - \left(1 + \frac{r^2 A_1^2}{4}\right)B_v \to (3.4)$$

$$(R_\sigma - a)H_r = a\,r\,H_{rr} - 2\,a\,r\,A_1 H_{rv} + \frac{a}{r}\left(1 + r^2 A_1^2\right)H_{vv}$$

$$\to (3.5)$$

$$T_r = \frac{1}{\mathrm{Re}\,\mathrm{Pr}}\left[(r\,aT_r - a\,rA_1 T_{\nu})_r - a\,A_1 T_{r\nu} + \frac{a(1+r^2)A_1^2}{r}T_{\nu\nu}\right]$$
$$+ \frac{R_H E_C}{a\,rR_\sigma}\left[a^2 r^2 H_r^2 - 2a^2 r^2 A_1 H_r H_\nu + a^2(1+r^2 A_1^2)H_\nu^2\right]$$
$$+ \frac{E_C \mu}{\mathrm{Re}}\left(\frac{A_1^2}{a\,r} + \frac{4}{a\,r^3}\right)$$
$$\rightarrow (3.6)$$

where

$$B = -\frac{4\mu}{a\,r^2 \mathrm{Re}} \qquad\qquad \rightarrow (3.7)$$

Equations (3.3) and (3.4) employing integrability condition $L_{\nu r} = L_{r\nu}$, yield

$$a\,r^3 A_1^2 B_\nu + a\,r^4 A_1^2 B_{r\nu} - (3\,A_1 a\,r^2 + 4\,a\,r^4 A_1^2)B_{\nu\nu}$$
$$= 4A_1 + a\,A_1 r^2 B + 2\,a\,A_1 r^3 B_r + a\,r^4 A_1 B_{rr} - 2\,a\,A_1^2 r^3 \, B_\nu$$
$$- (4a\,r^2 + a\,r^4 A_1^2)B_{\nu\,r}$$
$$\rightarrow (3.8)$$

A solution of equation (3.8) is

$$B = r^{-\frac{1}{2}}\left(C_1 \cos\frac{\sqrt{3}}{2}\ln r + C_2 \sin\frac{\sqrt{3}}{2}\ln r\right) - \frac{4}{3\,a^2 \, r^2} \quad \rightarrow (3.9)$$

provided B is a function of r alone. In equation (3.9) ,C_1 and C_2 are the non−zero arbitrary constants. Equation (3.7) , utilizing equation (3.9), yields

$$\mu = -\frac{a\,r^3 \mathrm{Re}}{4}\left(C_1 \cos\frac{\sqrt{3}}{2}\ln r + C_2 \sin\frac{\sqrt{3}}{2}\ln r\right) + \frac{\mathrm{Re}}{3a} \quad \rightarrow (3.10)$$

The solution of equation (3.5) is

$$H = C_3 \nu + C_4 Y(r) \qquad\qquad \rightarrow (3.11)$$

where

$$Y(r) = \begin{cases} \dfrac{A_1 C_3}{aC_4}(r\ln r - r) + C_5 r + C_6 \,` &, a = R_\sigma \;\;\rightarrow(3.12) \\[3mm] \dfrac{A_1 C_3}{C_4(a - R_\sigma)}r + \dfrac{C_7 a\,r}{R_\sigma} + C_8 &, a \ne R_\sigma \;\;\rightarrow(3.13) \end{cases}$$

and C_3 , C_4 , C_5 , C_6 , C_7 , C_8 are all non−zero arbitrary constants. Substituting equations (3.10) and (3.11) in equation (3.6), we find

$$T = C_9(a\psi + b) + Z(r) \qquad\qquad \rightarrow(3.14)$$

where

$$Z(r) = \begin{cases} \displaystyle\int\left[\int Q(r)dr\;\right]dr + C_{10}\,r + C_{11} \;\;, & a = \mathrm{RePr} \\[2mm] \hspace{3cm} \rightarrow (3.15) \\[3mm] \displaystyle\int r^{\left(\frac{\mathrm{RePr}}{a}-1\right)}\left[\int r^{\left(1-\frac{\mathrm{RePr}}{a}\right)}Q(r)dr\right]dr + \frac{aC_{12}}{\mathrm{RePr}}r^{\frac{\mathrm{RePr}}{a}} \\[3mm] + C_{13} \;\;, & a \ne \mathrm{RePr} \end{cases}$$
$$\rightarrow (3.16)$$

In equations (3.14−3.16) ,C_9 , C_{10} , C_{11} , C_{12} , C_{13} are all non−zero arbitrary constants, and

$$Q(r) = -\frac{R_H E_C \mathrm{RePr}}{R_\sigma a^2 r^2}\left[\begin{array}{l}a^2 r^2 C_4^2 Y'^2(r) - 2a^2 r^2 A_1 C_4 C_3 Y'(r) \\ + a^2 C_3^2\left(1 + r^2 A_1^2\right)\end{array}\right]$$
$$+ \frac{A_1 C_9}{r} - \frac{E_C \mathrm{Pr}\mu}{a\,r}\left(\frac{A_1^2}{a\,r} + \frac{4}{a\,r^3}\right)$$
$$\rightarrow (3.17)$$

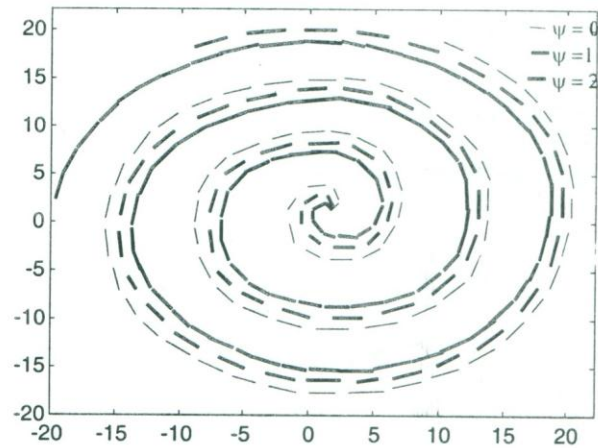The streamline pattern for this flow is shown in fig. 1.

Fig. 1 Streamline Pattern for $\theta - A_1\,r = \psi$

(II) We let the family of curves $\theta - A_1 r^2 - A_2 r =$ constant be the streamlines so that we have

$$\theta = A_1 r^2 + A_2 r + a\psi + b \qquad \rightarrow (3.18)$$

comparing equations (3.18) and (1.1), we get

$$f(r) = A_1 r^2 + A_2 r \qquad \rightarrow (3.19)$$

In equation (3.19) A_1 and A_2 are both non–zero arbitrary constants. On substituting equation (3.19) in equations (3.3–3.5), we get

$$L_r = \frac{A_1^2}{2} r^2 B + \frac{A_1^2}{2} r^3 B_r + \frac{A_1 A_2}{4} rB + \frac{A_1 A_2}{4} r^2 B_r \rightarrow (3.20)$$
$$+ \left[\frac{A_1}{4} - \frac{A_1}{4} r^2 (2A_1 r + A_2)^2 - (2A_1 r + A_2) \right] B_v$$

$$L_v = -\left(\frac{2A_1}{a^2} + \frac{A_2}{a^2 r} \right) + \frac{A_1}{4} B_r + \frac{A_1}{4} r^2 B_r -$$
$$\qquad\qquad \left[\frac{A_1^2 r^3}{2} + \frac{A_1 A_2 r^2}{4} + 1 \right] B_v \qquad \rightarrow (3.21)$$

$$R_\sigma H_r - a H_r = a r H_{rr} - 2 a r (2A_1 r + A_2) H_{rv}$$
$$+ \frac{a}{r} \left[1 + r^2 (2A_1 r + A_2)^2 \right] H_{vv} - (4A_1 r + A_2) H_v \qquad \rightarrow (3.22)$$

On eliminating the function L from equation (3.20) and (3.21), we get

$$\left(\frac{A_1^2}{2} r^2 + \frac{A_1 A_2}{4} r \right) B_v + \left(\frac{A_1^2}{2} r^3 + \frac{A_1 A_2}{4} r^2 \right) B_{rv}$$
$$+ \left[\frac{A_1}{4} - \frac{A_1}{4} r^2 (2A_1 r + A_2)^2 - (2A_1 r + A_2) \right] B_{vv}$$
$$= \frac{A_2}{a^2 r^2} + \frac{A_1 B}{4} + \frac{3A_1 r B_r}{4} + \frac{A_1 r^2 B_{rr}}{4} - \left(\frac{3A_1^2 r^2}{2} + \frac{A_1 A_2 r}{2} \right) B_v$$
$$- \left(\frac{A_1^2 r^3}{2} + \frac{A_1 A_2 r^2}{4} + 1 \right) B_{vr}$$
$$\rightarrow (3.23)$$

A solution of this equation is

$$B = \frac{1}{r} (d_1 + d_2 \ln r) - \frac{4A_2}{a^2 A_1 r^2} \qquad \rightarrow (3.24)$$

where d_1 and d_2 are both non–zero arbitrary constants. The function μ, on utilizing equation (3.7), is given by

$$\mu = \frac{ar \, \text{Re}}{4} (d_1 + d_2 \ln r) + \frac{A_2 \, \text{Re}}{aA_1} \qquad \rightarrow (3.25)$$

A solution of equation (3.22) is

$$H = d_3 v + d_4 S(r) \qquad \rightarrow (3.26)$$

where

$$S(r) = \begin{cases} \dfrac{4A_1 d_3}{2 a d_4} r^2 + \dfrac{A_2 d_3}{a d_4} r (\ln r - 1) + d_5 r + d_6 \;,\; a = R_\sigma \\ \qquad\qquad\qquad\qquad\qquad\qquad\qquad \rightarrow (3.27) \\[2ex] \dfrac{2A_1 d_3 r^2}{d_4 (2a - R_\sigma)} + \dfrac{A_2 d_3}{d_4 (a - R_\sigma)(2a - R_\sigma)} r^{\frac{2a - R_\sigma}{a}} \\ + d_7 r + d_8 \;,\; a \neq R_\sigma \\ \qquad\qquad\qquad\qquad\qquad\qquad\qquad \rightarrow (3.28) \end{cases}$$

and d_3, d_4, d_5, d_6, d_7, d_8 are all non–zero arbitrary constants. The solution of the equation (2.37), in this case, is

$$T = d_9 (a\psi + b) + Z(r) \qquad \rightarrow (3.29)$$

where

$$Z(r) = \begin{cases} r^{\frac{\text{Re Pr}}{a} - 1} \left[\int Q_1(r) r^{1 - \frac{\text{Re Pr}}{a}} \, dr \right] dr + \dfrac{d_{10} \, a}{\text{Re Pr}} r^{\frac{\text{Re Pr}}{a}} \\ + d_{11} \;, a \neq \text{RePr} \qquad\qquad \rightarrow (3.30) \\[2ex] \int \left\{ \int Q_1(r) \, dr \right\} dr + d_{12} r + d_{13} \;, \\ a = \text{RePr} \qquad\qquad\qquad\qquad \rightarrow (3.31) \end{cases}$$

$$Q_1(r) = \frac{(4A_1 r + A_2)d_9}{r} - \frac{E_C \mu Pr}{a^2 r}\left(\frac{A_2^{\,2}}{r} + \frac{4}{r^3}\right)$$

$$- \frac{R_H E_C RePr}{r^2 R_\sigma}\left[\begin{array}{l} r^2 d_4^{\,2} S'^{\,2}(r) - 2r^2(2A_1 r + A_2)d_3 d_4 S'(r) \\[4pt] + \left\{1 + r^2(2A_1 r + A_2)^2\right\}^2 d_3 \end{array}\right]$$

$$\rightarrow (3.32)$$

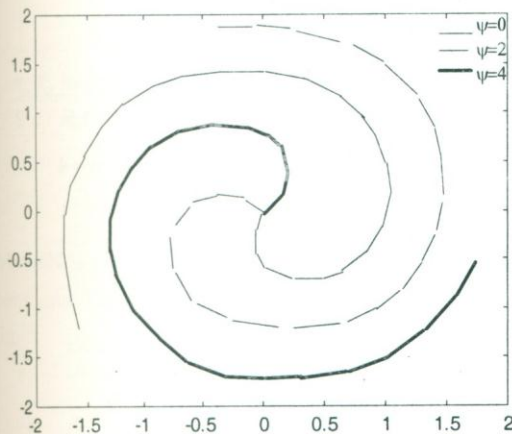and d_9 , d_{10}, d_{11}, d_{12} , d_{13} are all non−zero arbitrary constants. The streamline pattern for this flow is shown in fig. 2 .

Fig. 2 Streamline Pattern for $\theta - A_1 r^2 - A_2 r = \psi$

(III)   Flow with $\theta - A_1 r^3 - A_2 r^2 = $ constant as streamlines. In this case

$$f(r) = A_1 r^3 + A_2 r^2 \qquad\qquad \rightarrow (3.33)$$

and we find that

$$B = \frac{1}{r}\left(m_1 + m_2 \ln r\right) + \frac{12}{a^2}$$

$$\mu = -\frac{a r \, Re}{4}(m_1 + m_2 \ln r) - \frac{3 r^2 \, Re}{a}$$

$$H = m_3(a\psi + b) + m_4 Y(r)$$

$$Y(r) = \begin{cases} \dfrac{m_3}{m_4}\left(\dfrac{3A_1}{3a - R_\sigma}r^3 + \dfrac{2A_2}{2a - R_\sigma}r^2\right) + \dfrac{m_5\, a}{R_\sigma} r^{\frac{R_\sigma}{a}} \\[8pt] \quad + m_6 \quad, \quad a \ne R_\sigma \\[10pt] \dfrac{m_3}{a\, m_4}\left(\dfrac{3A_1}{2}r^3 + 2A_2 r^2\right) + m_7 r + m_8 \quad, \quad a = R_\sigma \end{cases}$$

$$T = m_9(a\psi + b) + Z_1(r)$$

$$Z_1(r) = \begin{cases} \displaystyle\int r^{\frac{Re\,Pr}{a}-1}\left[\int Q_1(r) r^{1-\frac{Re\,Pr}{a}}\,dr\right] + \dfrac{a\, m_{10}\, r^{\frac{Re\,Pr}{a}}}{Re\,Pr} \\[8pt] \quad + m_{11} \,, \; a \ne RePr \\[12pt] \displaystyle\int\left[\int Q_1(r)\,dr\right]dr + m_{12}\, r + m_{13} \quad, a = RePr \end{cases}$$

$$Q_1(r) = \frac{m_9}{r}\left(3A_1 r^2 + 2A_2 r\right) + \frac{E_C \mu\, Pr}{a^2 r}\left(9A_1^{\,2}r^3 + \frac{4}{r^3}\right)$$

$$+ \frac{R_H E_C\, Re\, Pr}{a\, r\, R_\sigma}\left[\begin{array}{l} a\, r\, m_4^{\,2} Y'^{\,2}(r) - 2\, a\, r\, m_3 m_4(3A_1 r^2 \\[4pt] + 2A_2 r)Y'(r) \\[8pt] + \dfrac{a\, m_3^{\,2}}{r}\left\{1 + r^2(3A_1 r^2 + 2A_2 r)^2\right\} \end{array}\right]$$

$$\rightarrow (3.34)$$

where m_i's (i = 1 , − − − − − −, 13) are all non−zero arbitrary constants.
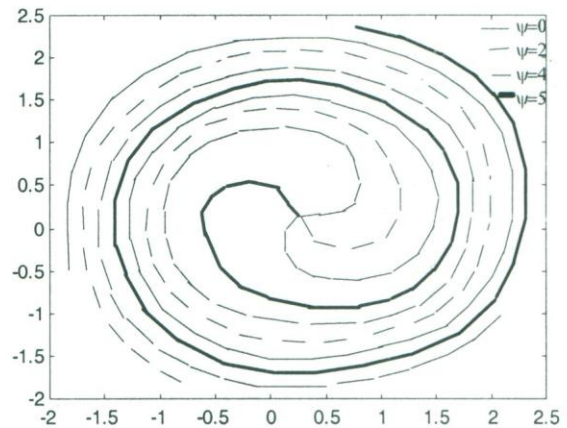
The streamline pattern for this flow is shown in fig. 3.

Fig. 3 Streamline Pattern for $\theta - A_1 r^3 - A_2 r^2 = \psi$

(IV) For the flow with $\theta - A_1 r^m =$ constant as streamlines $(m \neq 1)$, we find that

$$B = \frac{1}{r}(M_1 + M_2 \ln r) + A_1(m-2)r^{m-1}$$

$$\mu = -\frac{a\, r\, \mathrm{Re}}{4}(M_1 + M_2 \ln r) - \frac{a\, \mathrm{Re}\, A_1}{4}(m-2)r^{m+1}$$

$$H = M_4(a\psi + b) + M_5 Q_3(r)$$

$$Q_3(r) = \begin{cases} \dfrac{A_1 M_3 m}{a(m-1)M_4} r^m + M_5 r + M_6 \quad , \quad a = R_\sigma \\[4mm] \dfrac{A_1 m\, M_3 r^m}{M_4(a\,m - R_\sigma)} + \dfrac{M_7 a\, r^{\frac{R\sigma}{a}}}{R_\sigma} + M_8 \quad , \quad a \neq R_\sigma \end{cases}$$

$$T = M_9(a\psi + B) + Z_1(r)$$

$$Z_1(r) = \begin{cases} \int r^{\frac{\mathrm{Re\,Pr}}{a}-1}\left[\int Q(r) r^{1-\frac{\mathrm{Re\,Pr}}{a}}\right]dr + \dfrac{a\, M_{10}}{\mathrm{Re\,Pr}} r^{\frac{\mathrm{Re\,Pr}}{a}} \\[2mm] \quad + M_{11} \quad , \quad a \neq \mathrm{RePr} \\[4mm] \int\left[\int Q(r)dr\right]dr + M_{12} r + M_{13} \quad , \quad a = \mathrm{RePr} \end{cases}$$

$$Q(r) = A_1 m^2 M_9 r^{m-2} + \frac{E_C\, \mu\, \mathrm{Pr}}{a^2 r}\left(A_1 m^2 r^{m-2} - 2A_1 m\, r^{m-2} + \frac{4}{r^3}\right)$$

$$-\frac{R_H E_C\, \mathrm{Re\,Pr}}{a^2 r^2 R_\sigma}\begin{Bmatrix} a^2 r^2 M_4^2 Q_3^{'2}(r) - 2a^2 r^2 A_1 m\, r^{m-1} \\ M_3 M_4 Q'(r) \\ + a^2(1 + A_1^2 m^2 r^{2m})M_3^2 \end{Bmatrix}$$

$$\rightarrow (3.35)$$

where M_i's (i=1–13) are all non zero arbitrary constants. The streamline pattern for this flow is shown in fig. 4.

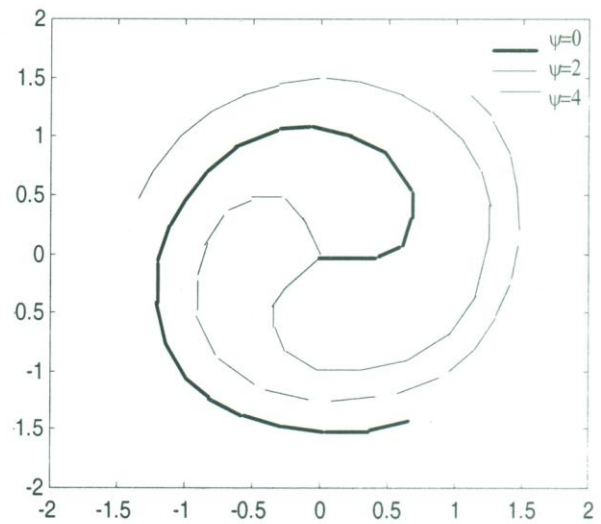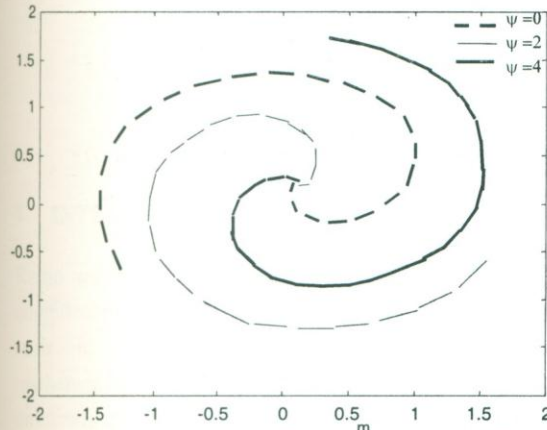

Fig. 4 Streamline pattern for $\theta - r^m = \psi$, $m = 4$

(V) For the streamlines pattern

$$\theta - A_1 r^m - A_2 \ln r = \text{constant} \quad , \quad \text{we find}$$

$$B(r) = \frac{1}{r}(N_1 + N_2 \ln r) + \frac{4m}{m-2} r^{m-3} - \frac{2A_2}{A_1 a^2} r^{-3}$$

$$\mu = -\frac{a\, r \mathrm{Re}}{4}(N_1 + N_2 \ln r) - \frac{m\, a \mathrm{Re} r^{m-1}}{m-2} + \frac{A_2 \mathrm{Re}}{2A_1 a\, r}$$

$$H = N_3(a\psi + b) + N_4 Y(r)$$

$$Y(r) = \begin{cases} \dfrac{A_1 N_3 m}{a\, N_4(m-1)} r^m + N_5 r + N_6 \quad , \quad a = R_\sigma \\[4mm] \dfrac{A_1 N_3 m\, r^m}{N_4(a\,m - R_\sigma)} + \dfrac{N_7 a\, r^{\frac{R\sigma}{a}}}{R_\sigma} + N_8 \quad , \quad a \neq R_\sigma \end{cases}$$

$$T = N_9(a\psi + b) + Z(r)$$

$$Z(r)=\begin{cases} \int r^{\frac{Re\,Pr}{a}-1}\left[\int r^{1-\frac{Re\,Pr}{a}}Q(r)dr\right]dr + \frac{aN_{10}}{Re\,Pr}r^{\frac{Re\,Pr}{a}} \\ \qquad + N_{11} \quad, a \neq Re Pr \\ \\ \iint\left[\int Q(r)dr\right]dr + N_{12}r + N_{13} \quad, a = Re Pr \end{cases}$$

$$Q(r) = A_1 m^2 N_6 r^{m-2} - \frac{E_C\,Pr\,\mu}{ar}\left[\frac{\left\{\left(m^2A_1 - 2mA_1\right)r^{m-1}-\frac{A_2}{r}\right\}^2}{ar} + \frac{4}{ar^3}\right]$$

$$+ \frac{R_H E_C\,Re\,Pr}{arR_\sigma}\left[a^2r^2N_4^2Y'^2 - 2a^2r^2N_3N_4\left(mA_1 r^{m-1}+\frac{A_2}{r}\right)Y' + a^2\left\{1+r^2\left(mA_1 r^{m-1}+\frac{A_2}{r}\right)^2\right\}N_3^2\right]$$

$$\rightarrow (3.36)$$

where N_i's $(i=1,2,\dots\dots13)$ are all non−zero arbitrary real constants. The streamline pattern for this flow is shown in fig. 5.

Fig. 5 Streamline pattern for $\theta - A_1 r - A_2(\ln r)=\Psi$, m=3

(VI) For the streamlines pattern

$$\theta - A_1(\ln r)^2 - A_2 \ln r = \text{constant}, \quad \text{we find}$$

$$\mu = -\frac{ar\,Re}{4}(D_1 + D_2 \ln r) + \frac{Re}{ar}(1+\ln r) + \left(\frac{A_2}{2aA_1}Re - \frac{Re}{2a}\right)\frac{1}{r}$$

$$H = \begin{cases} D_3(a\psi + b) - \frac{2A_1 D_3}{aD_4}\ln r + D_5 r + D_6 \quad, a = R_\sigma \\ \\ D_3(a\psi + b) + \frac{2A_1 D_3 r^{1-3a}}{D_4(3a-1)(R_\sigma + 2a)} + D_7 r^{\frac{R_\sigma}{a}-1} \\ \qquad\qquad\qquad + D_8 \quad, 3a \neq 1, a \neq R_\sigma \\ \\ D_3(a\psi + b) - \frac{2A_1 D_3 \ln r}{D_4(R_\sigma + 2a)} + D_7 r^{\frac{R_\sigma}{a}-1} \\ \qquad\qquad\qquad + D_9 \quad, 3a = 1, a \neq R_\sigma \end{cases}$$

where D_i's $(i=1,2,\dots\dots\dots\dots9)$ are all non−zero constants.

The temperature distribution, employing expression for f(r), μ and H(r) can easily be determined from equation (3.27) in similar manner as in previous examples.

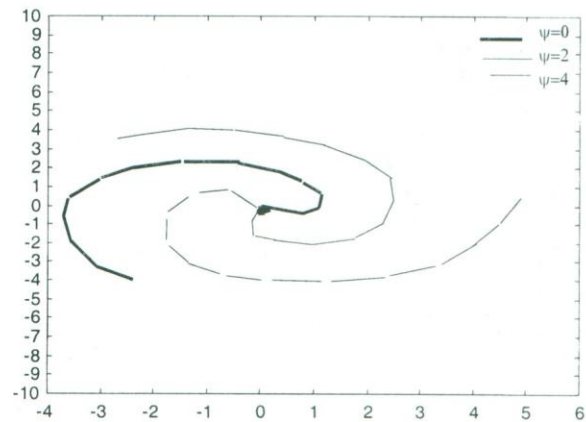The streamline pattern for this flow is shown in fig. 6.

Fig. 6 Streamline pattern for $\theta - A_1(\ln r)^2 - A_2 \ln r = \Psi$

4. CONCLUSIONS

In the present work the equations governing the motion of an incompressible fluid of variable viscosity in the presence of a transverse magnetic field are considered. Following Naeem and Nadeem, the equations are transformed into a new system of equations in the coordinate system (ϕ,ψ) in which ψ = constant represent streamline and ϕ = constant are left as a family

of arbitrary curves. By taking $\phi = r$, $x = r\cos\theta$, $y = r\sin\theta$ the flow equations in (ϕ, ψ) system are transformed in (r, ψ) system and exact solutions are determined for various flows characterized by the streamfunction defined in equation (1.1).

REFERENCES

[1]   M . H . Martin, The flow of a viscous fluid, I, Arch. Rational. Mech. Anal. 41 , 266 – 286 , 1971 .

[2]   R . K . Naeem and S . A . Nadeem, Study of steady plane flows of an incompressible fluid of variable viscosity using Martin's Method, Journal of Applied Mechanics and Engineering , Vol. 1 , No. 3 , pp . 397 – 434 , 1996 .

[3]   L. Prandtl, Ein GedanKenmodell zur, Kinetischen Theorie, der festen Ko''rper, ZAMM , Vol. 8, pp. 85 – 106 , 1928.

[4]   Poiseuille, Uber Reibungtropbarer Flussigketilen, Wein Sitzungsber, Vol. 10, pp. 607 , 1860.

[5]   F. Labropulu and O. P. Chandna., Exact solutions of steady plane flows using (r, Ψ)– coordinates, International J. Math and Math. Sci. , Vol. 23, No. 7, pp. 449 – 475, 2000 .

A UNIFIED FRAMEWORK FOR CHARACTERIZING FADING CHANNELS AND THEIR DETERMINISTIC SIMULATIONS: PART-1

Umrani A. Waheed[*]

ABSTRACT

To understand the complicated phenomena of radio propagation one has to understand the physical properties of underlying environment and careful modeling of the propagation phenomena. It is well knows that the signal coming to/from a mobile handset is reflected, refracted and scattered due to various obstacles, such as, large building, vegetation, moving objects etc., it come across. In this paper, we describe a framework to characterize the radio propagation models, usually called fading channels. The primary purpose of this paper is to briefly review the principal characteristics and models for fading channels and to help young engineers/students working in communication engineering understand the underlying phenomena behind the modeling. The underlying fading channel models are divided into two categories, namely, single-state channel models and multi-state channel models. Moreover, the author wants to give an emphasis on a new method of modeling and simulating the fading channels using deterministic processes, which is simple and easy to comprehend. Typically, the simulation models for fading channels are realized by employing two or more colored Gaussian noise processes. The traditional method for the design of colored Gaussian noise processes is to shape a white Gaussian noise (WGN) process by means of a filter that has a transfer function, which is equal to the square root of Doppler power spectral density of the fading process. Recently, a new method that is becoming more and more popular, based on Rice's sum of sinusoids is proposed. In this method, a colored Gaussian noise process is approximated by a finite sum of weighted and properly designed sinusoids. The advantages include less hardware expenditure (no need of filters), less simulation time, and above all the power spectral density is asymmetrical. The validity of latter method has been reported extensively in literature for real- world land mobile satellite channel models.

1. INTRODUCTION

Radio wave propagation through wireless channels is a complicated phenomenon characterized by various effects such as multi-path and shadowing. A precise mathematical description of this phenomenon is either unknown or too complex for tractable communications systems analyses. However, considerable efforts have been devoted to the statistical modeling and characterization of these effects. The result is a range of relatively simple and accurate statistical models for fading channels, which depend on the particular propagation environment and the underlying communication scenario.

This paper due to space limitations is divided into two parts. The first part is devoted to characterize the fading channels under a common framework, which helps us to simulate these models using a new technique called Deterministic Methods to generate random processes. The primary purpose of this paper is to briefly review the principal characteristics and models for fading channels and to help young engineers/students working in communication engineering understand the underlying phenomena behind the modeling in a simple and comprehensive way. A more detailed treatment of this

*   Lecturer, Department of ES & TL, Mehran University of Engineering & Technology, Jamshoro, Pakistan.

subject can be found in standard textbooks such as [1], [2]. Moreover, the author wants to give an emphasis on a new method of modeling the fading channels, which is simple and easy to comprehend.

The significance of the unified framework described is that almost all the statistical fading channels can be modeled and simulated with some exceptions. The author in [3], [4], [5] has not only used these method not only to simulate the complex fading channels but also evaluated the performance of wireless communications systems, including Low Earth Orbit (LEO) satellite communications and the latest space-time communications systems (e.g., MIMO) using multiple antennas. This paper is written in a simplified way to enable students of telecommunications engineering to understand the simulation architecture of fading channels models and their applications.

In the second part, bit error rate performance of space-time communication system using multiple antennas at both base station and mobile station of wireless communication systems is computed using the method of deterministic simulations.

Rest of the paper is organized as follows. The main characteristics and corresponding models of fading channels are presented in the next section 2. In section 3 a detail introduction is given on fading amplitude generation through deterministic processes. Finally, the chapter is concluded in section 4.

2. MOBILE FADING CHANNELS

In this section, we describe in detail the concept, types, classifications of fading channel models and their characterization.

Slow and Fast Fading: The distinction between slow and fast fading is important for the mathematical modeling of fading channels and for the performance evaluation of communication systems operating over these channels. This notion is related to the coherence time of the channel, defined as the inverse of the channel Doppler spread which measures the period of time over which the fading process is correlated. The fading is said to be slow if the symbol time duration is smaller than the channel's coherence time, otherwise it is considered to be fast. In slow fading a particular fade level will affect many successive symbols, which leads to burst errors, whereas in fast fading the fading is independent from symbol to symbol.

Frequency-Flat and Frequency-Selective Fading: Frequency-selectivity is also an important characteristic of fading channels. If all the spectral components of the transmitted signal are affected in a similar manner, the fading is said to be frequency-nonselective or equivalently frequency-flat. This is the case for narrow-band systems in which the transmitted signal bandwidth is much smaller than the channel's coherence bandwidth. This bandwidth is defined as the inverse of the maximum delay spread $\emptyset_{max}$, and measures the frequency range over which the fading process is correlated. On the other hand if the spectral components of the transmitted signal are affected by different amplitude gains and phase shifts, the fading is said to be frequency-selective. This applies to wide-band systems in which the transmitted bandwidth is bigger than the channel's coherence bandwidth.

2.1 SINGLE STATE MODELS

When fading affects narrow-band systems, the received carrier amplitude is modulated by the fading amplitude R, where R is a RV with mean square $\Omega = \overline{R^2}$ and probability density function PDF $p_R(R)$ which is dependent on the nature of the radio propagation environment. When passing through the fading channel, the signal is perturbed at the receiver by additive white Gaussian noise (AWGN) which is typically assumed to be statistically independent of the fading amplitude R, and which is characterized by a one-sided power spectral density N_o (W/Hz). The instantaneous received signal power is modulated by R^2. Thus we define the instantaneous signal-to-noise power ratio (SNR) per symbol by $\gamma = R^2 E_S/N_o$ and the average

SNR per symbol by $\bar{\gamma} = \Omega \dfrac{E_s}{N_o}$, where E_s r is the energy

per symbol. Performance evaluation of communication systems over fading channels will generally be a function of E_s/N_o or E_b/N_o. For slowly varying channels the fading amplitude is constant over a symbol time and the PDF of γ is obtained by introducing a change of variables in the expression for the fading PDF p_R (R) of R yielding.

$$p_\gamma(\gamma) = \frac{p_R\left(\sqrt{\frac{\Omega\gamma}{\bar{\gamma}}}\right)}{2\sqrt{\frac{\Omega\gamma}{\bar{\gamma}}}} \qquad \rightarrow (1)$$

Multi-path fading is due to the constructive and destructive combination of randomly delayed, reflected, scattered, and diffracted signal components. This type of fading is relatively fast and is therefore responsible for the short-term signal variations. Depending on the nature of the radio propagation environment, there are different models describing the statistical behavior of the fading envelope.

Rayleigh: This distribution is most frequently used to model multi-path fading with no direct line-of-sight (LOS) path. In this case, the channel fading amplitude R is distributed according to

$$P_\alpha(R;\Omega) = \frac{2R}{\Omega}\exp\left(-\frac{R^2}{\Omega}\right); \qquad R \geq 0, \qquad \rightarrow (2)$$

and hence the instantaneous SNR per symbol of the channel, γ, is distributed according to an exponential distribution given by

$$P_\gamma(\gamma) = \frac{1}{\bar{\gamma}}\exp\left(-\frac{\gamma}{\bar{\gamma}}\right); \qquad \gamma \geq 0, \qquad \rightarrow (3)$$

It also applies to the propagation of reflected and refracted paths through the troposphere and ionosphere [1], [8].

Nakagami-n (Rice): The Nakagami-n distribution is also known as the Rice distribution [1]. It is often used to model propagation paths consisting of one strong direct LOS component and many random weaker components. Here the channel fading amplitude follows the distribution

$$P_R(R;\Omega,n) = \frac{2(1+n^2)e^{-n^2}R}{\Omega}\exp\left(-\frac{(1+n^2)R^2}{\Omega}\right)I_0\left(2nR\sqrt{\frac{1+n^2}{\Omega}}\right); \; R \geq 0,$$
$$\rightarrow (4a)$$

where n is the Nakagami-n parameter which ranges from 0 to ∞ and which is related to the Rician factor by $K = n^2$.

$$P_R(R;\Omega,K) = \frac{2(1+K)R}{\Omega}\exp\left(-K-\frac{(1+K)R^2}{\Omega}\right)I_0\left(2R\sqrt{\frac{(1+K)K}{\Omega}}\right); \; R \geq 0,$$
$$\rightarrow (4b)$$

By simple transformation [1, eq. (2.42)] (4b) can be re-written as

$$P_R(R;\Omega) = \frac{2R}{\Omega}\exp\left(-\frac{(A_S^2+R^2)}{\Omega}\right)I_0\left(\frac{2A_S R}{\Omega}\right); \quad R \geq 0, \quad \rightarrow (4c)$$

where A_S is non-centrality parameter.

Applying (1) shows that the SNR per symbol of the channel γ, is distributed according to a non-central chi-square distribution given by

$$p_\alpha(\gamma,n) = \frac{(1+n^2)e^{-n^2}}{\bar{\gamma}}\exp\left(-\frac{(1+n^2)\gamma}{\bar{\gamma}}\right)I_0\left(2n\sqrt{\frac{(1+n^2)\gamma}{\bar{\gamma}}}\right); \; \gamma \geq 0,$$
$$\rightarrow (4)$$

It spans the range from Rayleigh fading (n = 0) to no fading (constant amplitude n = ∞). This type of fading is typically observed in the first resolvable LOS paths of micro-cellular urban and suburban land mobile, indoor environments [2]. It also applies to the dominant LOS path of satellite [6].

Nakagami-m: This pdf is in essence a central chi-square distribution given by [1], [2]

$$p_\alpha(R;\Omega,m) = \frac{2m^m R^{2m-1}}{\Omega^m \Gamma(m)} \exp\left(-\frac{mR^2}{\Omega}\right); \quad R \geq 0, \qquad \rightarrow (5)$$

where m is the Nakagami-m parameter which ranges from ½ to ∞. Applying (1) shows that the SNR per symbol, γ, is distributed according to gamma distribution given by

$$p_\gamma(\gamma; \bar{\gamma}, m) = \frac{m^m \gamma^{m-1}}{\bar{\gamma}^m \Gamma(m)} \exp\left(-\frac{m\gamma}{\bar{\gamma}}\right); \qquad \gamma \geq 0, \qquad \rightarrow (6)$$

Hence, the Nakagami-m distribution spans via the m parameter the widest range among all the multi-path distributions considered. For instance, it includes the one sided Gaussian distribution $(m=1/2)$ and the Rayleigh distribution $(m = 1)$ as special cases. In the limit as $m \rightarrow +\infty$, Nakagami-m fading channel converges to a non-fading AWGN channel.

The Nakagami-m distribution often gives the best fit to land-mobile [6] and indoor mobile channels [7].

Lognormal Shadowing: In terrestrial and satellite land-mobile systems, the link quality is also affected by slow variation of the mean signal level due to the shadowing from terrain, buildings, and trees. Communication system performance will depend only on shadowing if the radio receiver is able to average out the fast multi-path fading or if an efficient "micro"-diversity system is used to eliminate the effects of multi-path. Based on empirical measurements, there is a general consensus that shadowing can be modeled by a log-normal distribution for various outdoor and indoor environments [8], [9] in which case the path SNR per symbol γ has a PDF given by the standard lognormal expression

$$p_\gamma(\gamma; \mu, \sigma) = \frac{\xi}{\sqrt{2\pi}\sigma\gamma} \exp\left(-\frac{(10\log_{10}\gamma - \mu)^2}{2\sigma^2}\right); \qquad \rightarrow (7)$$

where $\xi = 10/\ln(10) = 4.3429$, and μ (dB) and σ (dB) are the mean and the standard deviation of $10\log_{10}\gamma$, respectively.

Composite Multi-path/Shadowing: A composite multi-path/shadowed fading environment consists of multi-path fading superimposed on lognormal shadowing. In this environment the receiver does not average out the envelope fading due to multi-path but rather reacts to the instantaneous composite multi-path/shadowed signal [1, Sec. 2.4.2]. This is often the scenario in congested down town areas with slow moving pedestrians and vehicles [10]. This type of composite fading is also observed in land-mobile satellite systems subject to vegetative and/or urban shadowing [11], [12]. There are two approaches and various combinations suggested in the literature for obtaining the composite distribution. Here, as an example, we present the composite gamma/lognormal PDF introduced by Ho and Stuber [1]. This pdf arises in Nakagami-m shadowed environments and is obtained by averaging the gamma distributed signal power (or equivalently the SNR per symbol) over the conditional density of the log-normally distributed mean signal power (or equivalently average the SNR per symbol), giving the following channel pdf.

$$p_\gamma(\gamma; m, \mu, \sigma) = \int_0^\infty \frac{m^m \gamma^{m-1}}{w^m \Gamma(m)} \exp\left(-\frac{m\gamma}{w}\right) \frac{\xi}{\sqrt{2\pi}\sigma w}$$
$$\exp\left(-\frac{(10\log_{10}w - \mu)^2}{2\sigma^2}\right) dw; \qquad \rightarrow (8)$$

2.2 TWO-STATE MODELS

From their land mobile satellite channel characterization experiments, Lutz et al. [12] and Barts and Stutzman [13] found that the overall fading process for land mobile satellite systems (LMSS) is a convex combination of un-shadowed multi-path fading and a composite multi-

path/shadowed fading. Here, as an example, we present in more detail the Lutz et al. model [12]. When no shadowing is present, the fading follows Rice (Nakagami-n) PDF. On the other hand when shadowing is present, it is assumed that no direct LOS path exists and the received signal power (or equivalently SNR per bit) is assumed to be an exponential/log-normal. The combination is characterized by the shadowing time-share factor, which is denoted by B, $O<B<1$; hence, the resulting combined PDF is given by

$$P_{AK\sigma}(\gamma\gamma B, \gamma^{-u}, K; \mu^S, \sigma) = (1-B).p_n(\gamma\gamma\gamma^{-u}, K) + B.p_{m\sigma}(\gamma\gamma; 1\mu^S, \sigma)$$

$$\rightarrow(9)$$

where γ^u is the average SNR per symbol during the un-shadowed fraction of time, and μ^S is the average of $10\log_{10}\gamma$ during the shadowed fraction of time. The overall average SNR per symbol γ, is then given by

$$\overline{\gamma} = (1-B)\gamma^{-u} + B10^{\frac{\mu^S}{10} + \frac{\ln10\sigma^2}{200}}$$

$$\rightarrow(10)$$

2.3 THREE – STATE MODEL

Karasawa in [14], proposed a three-state channel model. In this model, the signal in each state (i.e. states A, B and C) is combined by two factors: direct wave component "a" and mutipath component "b". The factor "a" can be categorized in three classes, that is, a_1 denotes the direct wave component without shadowing; a_2 denotes component with slight shadowing and a_3 denotes the direct component with perfect shadowing. The factor "b" can also be categorized in two classes, b_1 represents specular mutipath wave component on the ground and b_2 represents scattered wave components. The two sub-classes of "b" can be considered totally. Hence state A, B, and C is defined by the combinations of a_1 and b, a_2 and b, and a_3 and b, respectively, as shown in Fig. 1.
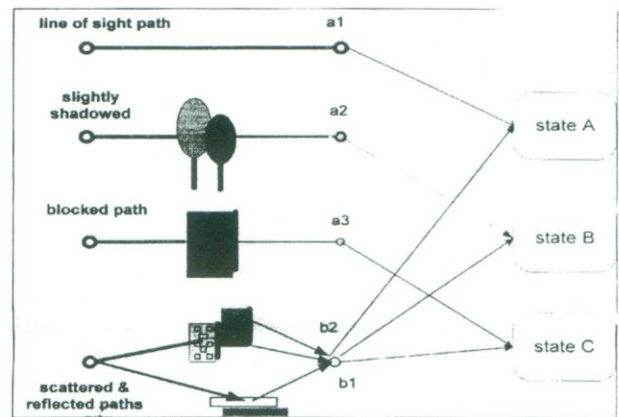

Fig. 1 Three States Channel Model

State A is represented by Rician model, which describes signal with constant direct wave component and Rayleigh distributed scattered components. State B coincides well with superimposed lognormal/Nakagami-*m* model. State C, can be represented by Rayleigh fading model described in section 2.1. So the pdf of each state can be represented by

$$P_A(R;\Omega_A) = \frac{2R}{\Omega_A}\exp\left(-\frac{(A_S^2 + R^2)}{\Omega_A}\right)I_0\left(\frac{2A_SR}{\Omega_A}\right); \quad R \geq 0, \rightarrow(11a)$$

$$P_B(R;\Omega_B,\mu,\sigma) = \frac{6.930R}{\sigma\Omega_B}\int_0^\infty\frac{1}{w}\exp\left(-\frac{(20\log_{10}w - \mu)^2}{2\sigma^2} - \frac{(w^2 + R^2)}{\Omega_B}\right)I_0\left(\frac{2wR}{\Omega_B}\right)dw;$$

$$\rightarrow(11b)$$

$$P_C(R;\Omega_C) = \frac{2R}{\Omega_C}\exp\left(-\frac{R^2}{\Omega_C}\right); \quad R \geq 0, \rightarrow(11c)$$

The overall pdf of the three-state model is given by

$$p(R) = P_A.P_A(R;\Omega_A) + P_B.P_B(R;\Omega_B,\mu,\sigma) + P_C.P_C(R;\Omega_C) \quad R \geq 0;$$

$$\rightarrow(12)$$

where P_A, P_B, and P_C denote the probability of state A, B, and C, respectively. The total probability must satisfy the condition that is $P_A + P_B + P_C = 1$.

From functional point of view, the three-state model formulated above includes most of the models presented in our discussion.

3. DETERMINISTIC METHODS

In general the simulation model for fading channels are realized by employing two or more colored Gaussian noise processes. The traditional method for the design of colored Gaussian noise processes is to shape a white Gaussian noise (WGN) process by means of a filter that has a transfer function, which is equal to the square root of Doppler Power Spectral Density (PSD) of the fading process [1].

Recently, a new method that is becoming more and more popular, based on Rice's sum of sinusoids is proposed by [15]. In this method, a colored Gaussian noise process is approximated by a finite sum of weighted and properly designed sinusoids. The advantages include less hardware expenditure (no need of filters), less simulation time, and above all the power spectral density is asymmetrical. The validity of latter method has been reported extensively in literature for real-world land mobile satellite channel models.

In [3], [4] the author has used deterministic methods to generate fading channel models and analyze the performance of direct sequence code division multiple access (DS CDMA) systems for Low Earth Orbit (LEO) satellite channels. The brief introduction to these processes is given in [14]. Further, in [5], the authors again demonstrate its simulation superiority by modeling a multi-input multi-output (MIMO) communications systems, which is considered the future of wireless communications beyond the third-generation (3G), systems. Specifically, the authors in [5] first characterize a MIMO channel model based on spatial fading correlation matrix, that is suitable for multi-antenna

communications environment and then generate the fading correlation matrix using deterministic methods. The details of the simulations will be covered in the second part of this paper.

A Rice process, $\xi(t)$, is defined by taking the absolute value of a nonzero mean complex Gaussian process

$$\xi(t) = \left| \mu_\rho(t) \right| = \left| \mu(t) + m(t) \right| \qquad \rightarrow (13)$$

where

$$\mu(t) = \mu_1(t) + \mu_2(t) \qquad \rightarrow (14)$$

$$m(t) = m_1(t) + jm_2(t) = \rho e^{j(2\pi(f_\rho t + \theta_\rho))} \qquad \rightarrow (15)$$

In (13), all scattered components in the received signal, are represented by a zero-mean complex Gaussian noise process with uncorrelated real components $\mu_i(t), i=1,2$, and variance $Var\{\mu(t)\} = 2Var\{\mu_i(t)\} = 2\sigma_\mu^2$ whereas the influence of direct line-of-sight (LOS) component is taken into account here by a time-variant mean value of the form denoted by $m(t)$, where, amplitude, Doppler frequency, and phase of the direct components are denoted by ρ, f_ρ, and θ_ρ, respectively. Observe that for $f_\rho=0$ the mean value $m(t) = m = \rho e^{i\theta_\rho}$ is obviously time-invariant, which directly corresponds to orthogonality between direction of the incoming wave component at the receiving antenna of the vehicle and the direction of the vehicle movement.

A typical and often assumed shape for Gaussian PSD of the complex Gaussian noise process $\mu(t)$, is given by Jakes PSD [1],

$$S_{\mu\mu}(f) = \begin{cases} \dfrac{2\sigma_0^2}{\pi f_{max} \sqrt{1 - (f/f_{max})^2}}, & |f| \le k_0 f_{max} \\[4mm] 0, & |f| > k_0 f_{max} \end{cases} \qquad \rightarrow (16)$$

Where f_{max}, is the maximum Doppler frequency and k_o ($0 < k_o < 1$) is an asymmetry parameter.

For $k_o = 1$, the classical Jakes PSD is obtained. For $0 < k_o < 1$, a so-called restricted Jakes Doppler PSD results. The resulting structure of the analytical model for Rice process with underlying Jakes PSD characteristics is shown in Fig. 2.
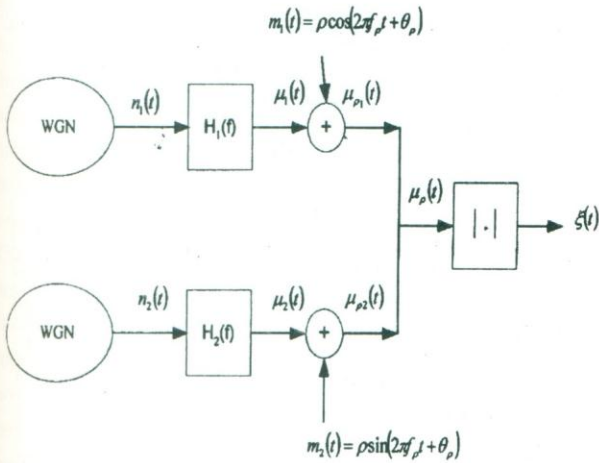

Fig. 2: Stochastic Analytical Model for Rice Processes with Jakes PSD

There are several methods to realize deterministic processes. In our simulation we use the method of Exact Doppler Spread [23], where a detailed introduction into the theory of deterministic simulation system can be found. Let us proceed by considering the two real functions $\mu_1(t)$ and $\mu_2(t)$, which are expressed as

$$\mu_i(t) = \sum_{n=1}^{N_i} C_{i,n} \cos(2\pi o_{i,n} t + \theta_{i,n}), \quad i = 1,2 \quad \rightarrow(17)$$

where N_i denotes the number of sinusoids of the function $\mu_i(t)$. The variables $C_{i,n}$, $f_{i,n}$, and $\theta_{i,n}$ are simulation model parameters which are adapted to the desired Doppler PSD function, and are therefore called Doppler coefficients, discrete Doppler frequencies, and Doppler phases, respectively. It is worth mentioning that

simulation model parameters have to be computed during the simulation setup, which saves substantial amount of time.

We use the method of Exact Doppler Spread [13] to compute parameter $C_{i,n}$, $f_{i,n}$, and $\theta_{i,n}$. The application of this method to the restricted Jakes PSD results in following closed-form expression for discrete Doppler frequencies $f_{i,n}$,

$$f_{i,n} = f_{max} \sin\left[\frac{\pi}{2N_1'}\left(n - \frac{1}{2}\right)\right], \quad n = 1, 2, ..., N_i \quad \rightarrow(18)$$

$$\text{where} \quad N_i' = \left[\frac{N_1 \pi}{(2\arcsin k_0)}\right].$$

where $0 < k_o < 1$. The corresponding Doppler coefficients $C_{i,n}$ are given by

$$c_{i,n} = \sigma_0 \sqrt{\frac{2}{N_i}}, \quad i = 1, 2 \ \& \ \text{for} \ n = 1, 2, ..., N_i \quad \rightarrow(19)$$

Finally, the Doppler phases $\theta_{i,n}$ are combined to a vector $\theta_i = (\theta_{i,1}, \theta_{i,2}, ..., \theta_{i,Ni})$, where the elements of this vector are identified with a permutation of the elements of the vector

$$\theta_i = \left[\frac{2\pi}{(N_i + 1)}, \frac{2\pi.}{(N_i + 1)}, ..., \frac{2\pi. i}{(N_i + 1)}\right] \quad \rightarrow(20)$$

for $i = 1,2$

Thus, all the parameters, $C_{i,n}$, $f_{i,n}$, and $\theta_{i,n}$, which define the behavior of (17), are determined by using deterministic method.

The functional block diagram representations of these fading channel models are shown in Figures 2- 4. In Figure 2, a traditional representation is shown, this model generate Rice processes, that also include state A and state C of the three state channel model described in

section 2.3, depending on the choice by varying the $m(t)$, which is the LOS component. Specifically, if there is no direct LOS of component it is assumed zero.

The underlying deterministic structure of Rice processes in Fig. 2, is shown in Fig. 3. One can find the difference which is obvious from its functional diagram. In a similar manner the deterministic model for state B, which is nothing but the Lognormal/Nakagami-m model is shown in Fig. 4.
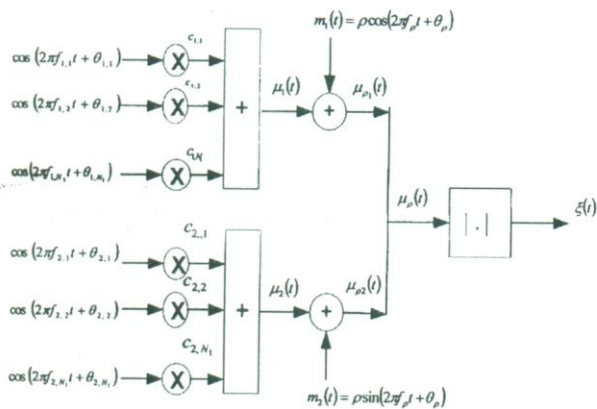

Fig. 3 Deterministic Simulation Model for Rice Processes with Jakes PSD
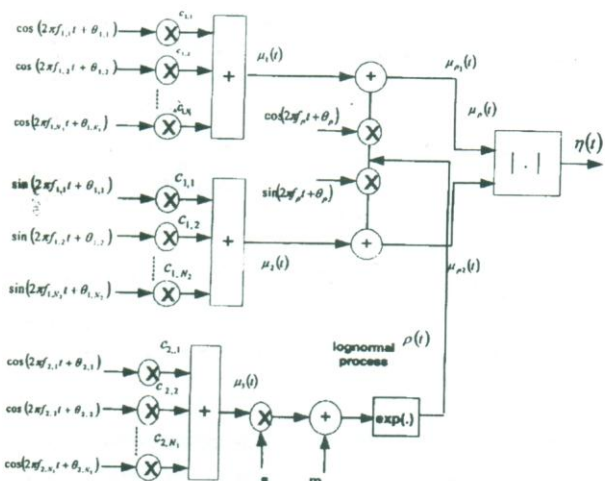
Fig. 4 Deterministic Simulation Model for State B (Loo's Model).

As an example we simulated the Rayleigh Fading Channel using the deterministic methods detailed above for slow and fast fading scenarios as shown in Figure 5-6. In Fig. 5, slow fading Rayleigh channel is simulated for f_m=20 Hz. Specifically 10000 samples were generated in Matlab 6.5. Similarly for fast fading channel with higher maximum Doppler frequency of 100 Hz, 100000 samples were simulated to plot fast Rayleigh fading channel as shown in Fig. 6. To a general reader the figures look similar, but that is not the case, if you carefully see the x-axis for both slow and fast fading channels, one can easily find the said difference.
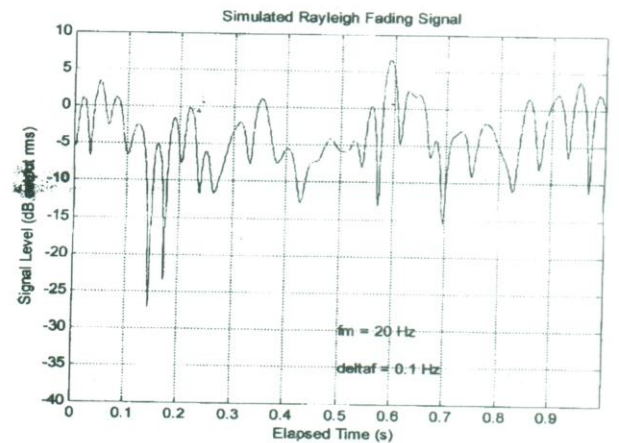

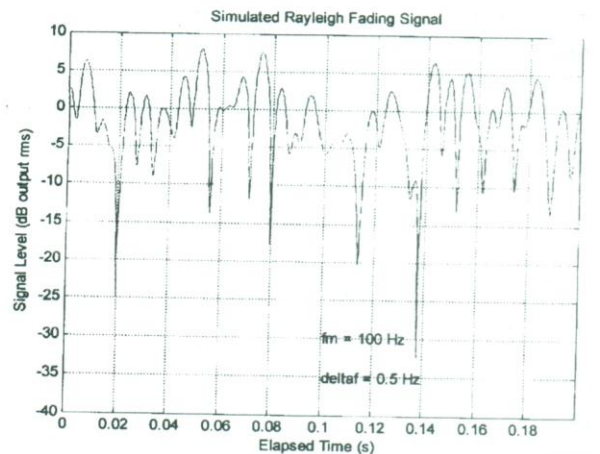Fig. 5 Simulated Rayleigh Fading Signal; Slow Fading (f_m=20Hz)

Fig. 6 Simulated Rayleigh Fading Signal; Fast Fading (f_m=20Hz).

4. CONCLUSION

In this paper, we describe a framework to characterize the radio propagation models, usually called fading channels. We first briefly reviewed the principal characteristics and models for fading channels that help young engineers/students working in communication engineering understand the underlying phenomena behind the modeling. The underlying fading channel models are divided into two categories, namely, single-state channel models and multi-state channel models. Specifically, a three state model is developed and described in detail, which includes almost all the channel models proposed in literature. A new method of modeling and simulating the fading channels using deterministic processes, which is simple and easy to comprehend, is described in detail. The traditional method for the design of colored Gaussian noise processes is to shape a white Gaussian noise (WGN) process by means of a filter that has a transfer function, which is equal to the square root of Doppler power spectral density of the fading process. Recently, a new method that is becoming more and more popular, based on Rice's sum of sinusoids is proposed. In this method, a colored Gaussian noise process is approximated by a finite sum of weighted and properly designed sinusoids. The advantages include less hardware expenditure (no need of filters), less simulation time, and above all the power spectral density is asymmetrical. We also give some examples, simulating the Rayleigh fading channel model for slow and fast fading respectively. The validity of these methods has been reported extensively in literature for real-world fading channel models.

ACKNOWLEDGEMENT

REFERENCES

[1] Stuber G. S, "Principles of Mobile Communications," Kluwer Academic Publishers: Norwell, MA USA 1996.

[2] Rappaport, T. S., "Wireless Communications; principles and practices," Prentice Hall PTR, NJ USA 2002.

[3] Umrani A. W., "DS CDMA system performance over a LEO Satellite channel" MUET Research Journal of Engg. & Tech., vol. 22, No. 1, Jan 2003 (ISSN 0254- 7821), pp. 1-11.

[4] Umrani A. W., Dubey V. K., and Choudhry B. S., "Dual Diversity Performance S CDMA system performance over a LEO Satellite channel" MUET Research Journal of Engg. & Tech., vol. 23, No. 3, July 2004 (ISSN 0254-7821).

[5] Umrani A. W. and Dubey V. K., "Deterministic simulation of spatial fading correlation for MIMO communication channels", Proc. IEEE International Multi-topic Conference on Information and Communications, INMIC 2003, Islamabad, Pakistan, 8-9 Dec. 2003, TB2 Pres- 65.

[6] Maral G., et al., "Satellite Communication Engineering," John Wiley, USA 2003.

[7] A. U. Sheikh, M. Handforth, and M. Abdi, "Indoor mobile radio channel at 946 MHz: measurements and modeling," Proc. IEEE Vehicular Tech. Conf. VTC'93, Secaucus, NJ, USA, pp. 73-76 May 1993.

[8] P. Yegani and C. McGlilem, " A statistical model for the factory radio channel," IEEE Trans. Commun., vol. COM-39, pp. 1445-1454, October 1991.

[9] H. Hashemi, "Impulse response modeling of indoor radio propagation channels," IEEE J. Select. Areas in Commun., vol. SAC-II, pp. 967-978, Sept. 1993.

[10] M. J. Ho, Stuber G. L., "Co-channel interference of micro-cellular systems on shadowed Nakagami fading channels," Proc. IEEE Vehicular Tech. Conf VTC'93, Seraucus NJ, USA, pp. 568-571, May 1993.

[11] Corazza G., Vatalaro F., "A statistical model for land mobile satellite channels and its application to non-geostationary orbit systems," IEEE Trans. on Vehicular Tech., vol. VT-43, pp. 738-742, August 1994.

[12] E. Lutz et al., "The Land Mobile Satellite Communication Channel- Recording, Statistics and Channel Model," IEEE Trans. on Vehicular Tech., vol.40, No.3, pp. 375-386 May 1991.

[13] Barts M., and Stutzman W. L. "Modeling and simulation of mobile satellite propagation," IEEE Trans. on Antennas Propagation vol., AP-40, pp. 375-382, April 1992.

[14] Y. Karasawa, K. Kazuhiro, and K. Minamissono, "Analysis of availability improvement in LMSS by means of satellite diversity based on three-state propagation model," IEEE Trans. on Vehicular Tech., vol. 46, No.4 pp. 1047-1056, November 1997.

[15] Patzold M., "Mobile Fading Channel," John Wiley & Sons, UK, 2002.

FUNDAMENTAL STRUCTURAL PROPERTIES OF COMPACTED BACKED CLAY SPECIMENS

Mahmood Memon[*] and Abdul Aziz Ansari[**]

ABSTRACT

In continuation with preliminary experimental study for determination of structural properties of baked clay specimens, the detail of which is presented elsewhere, more investigations have been carried out by testing cubes, which were compacted by applying compression of varying intensity. The specific gravity of these specimens was first determined. Then the specimens were baked and tested for finding crushing as well as tensile strength. Percentage of pit sand is clay and compressive force for compaction were the two major parameters. The results show reasonable improvement of strength with the increase of compacting force, which compares well with cement concrete. The maximum compressive strength upto 27.61 N/mm^2 (3950 psi) was achieved when the compacting force was 6 N/mm^2. This is much more than common cement concrete used for RCC work, for which cube crushing strength of 20 N/mm^2 (approx. 3000 psi) is acceptable. Thus, the results hold promise for possibility of making and using relatively cheaper pre-cast-baked clay post-reinforced structural members for construction of buildings in plains of Pakistan where chief materials of construction locally available are common clay and pit-sand.

1. INTRODUCTION

For long time porosity of manually manufactured common baked clay bricks and their other inherent defects retarded the idea of the use of pre-cast earthen panels for durable construction of reasonably good quality buildings. However, sky-rocketing cost of items like cement and reinforcement bars has reinvigorated the efforts to find cheaper alternatives of particularly cement concrete. The encouraging results of preliminary study conducted earlier [1] supported the notion that proper compaction, particularly through the use of simple, more efficient, swift and effective mechanized methods could pave the way for manufacture of preperforated post-reinforced baked clay structural panels for construction of multistorey buildings more economically without

sacrificing the quality or durability.

The economy can be achieved on several counts such as;

(i) Availability of this material locally as compared to industrial production like cement.

(ii) Mass scale production with mechanized method.

(iii) Saving in terms of plastering, finishing or applying paints and distempers etc with proper and uniform burning giving it a naturally good appearance, colour and texture. However, before embarking on such an ambitious plan it was deemed absolutely essential to study the

* Professor, Department of Civil Engineering, QUEST, Nawabshah, Sindh, Pakistan.
** Associate Professor, Department of Civil Engineering, QUEST, Nawabshah, Sindh, Pakistan.

various means of compaction and the extent of improvement of structural / strength properties which could be attained comfortably. Therefore, programme of study was chalked out the details of which are presented in the following sections.

2. DETAILS OF EXPERIMENTAL WORK

Cubes of 100 mm size were cast and tested. The major variables were the ratio of clay with pit-sand which ranged between 00 to 60% and the other major variable was compressive force which ranged between 00 to 6 N/mm^2 with an increment of 1 N/mm^2. The quantity of water content was maintained at 18%. The compaction was achieved with the help of universal load testing machine where the rate of loading was reasonably high. The mould was specially made from a very thick steel plate with top collar extended beyond 100 mm by about 40 mm so that the final size of the specimen would not be less than the required one. Special plunger was also got manufactured from 30 mm thick steel plate to apply the compressive force. Since the mould was very stiff, the compressive loading caused no distortions. It must be mentioned here that the clay was pulverized before mixing so that it could be used in microfined state. The specimens were first allowed to dry in the air under the shed for about three weeks. Then they were placed in an oven at a constant temperature of 105 ^{0}C for 24 hours. The shrinkage, specific weight and the specific gravity were then determined. Afterwards the models were baked and the two major properties i.e. cube crushing strength and tensile strength were determined.

3. ANALYSIS OF RESULTS

From table 1, it can be observed that the maximum shrinkage of the models was 2% when the compacting force was either zero or its intensity was very low. However, with the increase of compacting force the shrinkage reduced to 1%. Even this is quite considerable for pre-cast panels. Therefore, more force is required to reduce this to an acceptable level. The compacting force has pronounced effect on the specific weight which increases from 17.59 KN/m^3 to a value of 22.36 KN/m^3 for pure clay corresponding to specific gravity of 2.32. These values can be compared with 24 KN/m^3 and 2.65 respectively for normal cement concrete. An over all increase of 27% is obtained when the compacting force is increased from zero to 6 N/mm^2.

Table 2 gives details of crushing strength for all the cubes tested in the laboratory and percentage improvement of strength as a function of percentage of pit-sand when compared with that of pure clay. The values entered here are averaged for three specimens. Altogether 147 cubes were cast, baked in kiln at uniform temperature and were tested. This table shows that a maximum cube crushing strength of 27.61 N/mm^2 (3950 psi) is achieved when the pit-sand is 30% and the compacting force is 6 N/mm^2. This may be compared with common cement concrete of 1:2:4 mix ratio for which guaranteed cube crushing strength is taken as 20 N/mm^2 (3000 psi) [2-5].

From this table it can be observed that the compressive strength is the lowest when cubes are made of pure clay without compaction. The addition of pit sand seems to have reasonably good effect on strength properties upto about 30%, beyond which it has but very little influence on the compressive strength.

From table 2, it is also obvious that a maximum improvement of 68.45 percent is achieved when the ratio of pit-sand is 30 percent.

Table 1: Percentage of Shrinkage, Specific Weight & Specific Gravity

Level of Compression N	Pure Clay			Pure Clay + 10% Pit-Sand			Pure Clay + 20% Pit-Sand			Pure Clay + 30% Pit-Sand			Pure Clay + 40% Pit-Sand			Pure Clay + 50% Pit-Sand			Pure Clay + 60% Pit-Sand		
	%age of Shrinkage	Specific weight KN/m³	Specific Gravity	%age of Shrinkage	Specific weight KN/m³	Specific Gravity	%age of Shrinkage	Specific weight KN/m³	Specific Gravity	%age of Shrinkage	Specific weight KN/m³	Specific Gravity	%age of Shrinkage	Specific weight KN/m³	Specific Gravity	%age of Shrinkage	Specific weight KN/m³	Specific Gravity	%age of Shrinkage	Specific weight KN/m³	Specific Gravity
00	02	17.59	1.79	03	17.63	1.79	03	18.77	1.91	02	18.13	1.84	02	18.64	1.90	02	19.01	1.93	01	17.83	1.81
10000	02	19.49	1.98	02	19.30	1.96	02	19.52	1.99	02	19.63	2.00	02	19.49	1.98	02	19.18	1.95	02	18.65	1.90
20000	02	20.19	2.05	02	19.32	1.97	02	19.99	2.03	02	20.09	2.04	02	20.19	2.05	02	19.85	2.02	01	19.28	1.96
30000	02	20.83	2.12	02	19.93	2.03	02	20.33	2.07	02	20.98	2.13	02	20.83	2.12	01	20.51	2.09	01	20.10	2.04
40000	01	22.31	2.27	02	21.49	2.19	02	21.64	2.20	02	22.17	2.26	01	22.31	2.27	01	20.90	2.13	01	20.84	2.12
50000	01	22.33	2.27	01	21.86	2.22	02	22.18	2.26	02	22.40	2.28	01	22.3	2.27	01	21.48	2.19	01	20.91	2.13
60000	01	22.36	2.28	01	22.83	2.32	01	23.17	2.36	01	23.06	2.35	01	23.36	2.38	01	22.43	2.28	01	21.28	2.16

Table 2: Percentage Improvement of Cube Crushing Strength Versus Percentage of Pit-Sand

Load N	Pure Clay N/mm²	Pure clay + 10% Sand N/mm²	%age Diff:	Pure clay + 20% Sand N/mm²	%age Diff:	Pure clay + 30% Sand N/mm²	%age Diff:	Pure clay + 40% Sand N/mm²	%age Diff:	Pure clay + 50% Sand N/mm²	%age Diff:	Pure clay + 60% Sand N/mm²	%age Diff:
00	11.63	12.51	7.56	12.97	11.52	13.41	15.30	13.57	16.68	14.01	20.46	14.00	20.37
10000	11.83	12.72	7.52	13.27	12.17	13.37	13.01	14.11	19.27	15.57	31.61	15.11	27.72
20000	12.27	16.90	37.73	16.60	35.28	16.21	32.11	16.64	35.61	16.93	37.97	15.27	24.44
30000	12.46	18.17	45.82	18.94	52.00	18.40	47.67	22.25	78.57	18.13	45.50	18.94	52.00
40000	13.21	20.42	54.57	20.87	57.98	21.93	66.01	23.37	76.91	23.92	81.07	18.23	38.00
50000	15.85	25.40	60.25	23.51	48.32	24.57	55.01	25.11	58.42	25.47	60.69	20.17	27.25
60000	16.39	27.57	68.21	26.83	63.69	27,61	68.45	27.23	66.13	25.93	58.20	22.53	37.46

Figure 1 shows the relationship of cube crushing strength versus pit-sand ratio. From the Figure it can be observed that use of higher ratio of pit-sand causes substantial reduction of strength.

Table 3, which gives account of percentage improvement of cube crushing strength versus compacting load. It can be observed that a maximum improvement is achieved when pit-sand is 10% and compression is 6 N/mm^2. Steady improvement of cube crushing strength is obtained in all the cases as the compacting force increases. This implies that the compacting load should be increased further beyond this limit of 6 N/mm^2 to a level where curve showing cube crushing strength versus compacting force would become asymptotic.
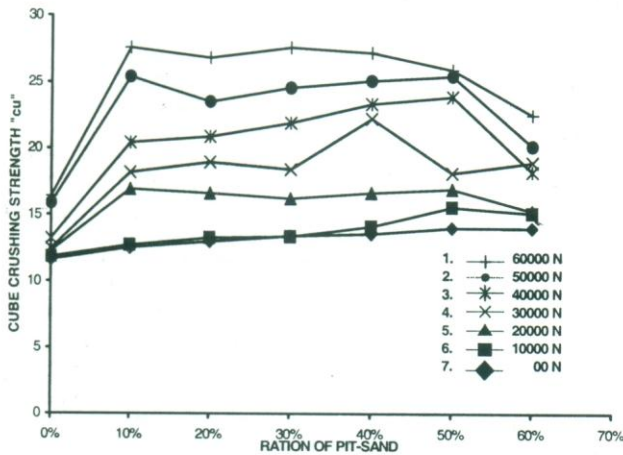
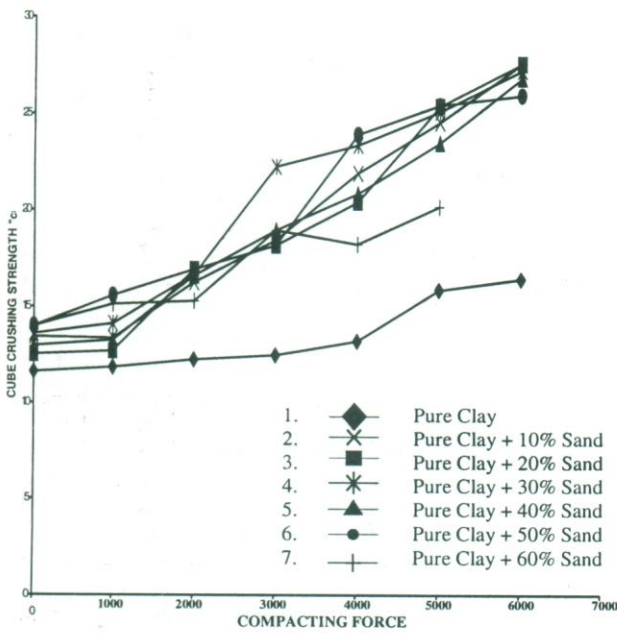Fig. 1 Cube Crushing Strength Versus Pit-Sand Ratio

Fig. 2 Cube Crushing Strength Versus Compacting Force

Figure 2, presents the behaviour of cube crushing strength as function of applied compacting force. From this figure it is very clear that there exists a possibility of further improvement of cube crushing strength if the compacting force is increased.

Table 4, shows the details of tensile strength baked clay specimens determined directly. Here cubes were first cast, compacted and baked. Then they were cut into thiner tiles and finally were given the shape of briquettes. The briquettes were then tested using Baileys Lever Arm Machine.

From table 4 several facts are self- evident, such as

(i)   For pure clay the tensile strength is approximately/ averagely 21% of cube crushing strength.

(ii)   Marked reduction of tensile strength take place as the ratio of pit-sand is increased. This actually alludes that the ratio of pit-sand should be in the range of only 10% to 20%.

(iii)   The tensile strength as a percentage of cube crushing strength becomes lower as the compacting force increases. However, in real terms the value as N/mm^2 increases with the increase of this force.

(iv)   As percentage of cube crushing strength, tensile strength is the lowest i.e. 6.32% when pit-sand is 50% and compacting load is 5 N/mm^2.

Table 3: Percentage Improvement of Cube Crushing Strength Versus Compacting Force.

Load "N" / %age difference	Pure Clay	Pure Clay + 10% Sand	Pure Clay + 20% Sand	Pure Clay + 30% Sand	Pure Clay + 40% Sand	Pure Clay + 50% Sand	Pure Clay + 60% Sand	
00	11.63	12.51	12.97	13.41	13.57	14.01	14.00	N/mm²
10000	11.83	12.72	13.27	13.37	14.11	15.57	15.11	N/mm²
%age difference	1.71	1.67	2.31	-0.29	3.97	11.13	7.92	%
20000	12.27	16.90	16.60	16.21	16.64	16.93	15.27	N/mm²
%age difference	5.50	35.09	27.98	20.87	22.62	20.84	9.071	%
30000	12.46	18.17	18.94	18.40	22.25	18.13	18.94	N/mm²
%age difference	7.14	45.24	46.03	37.21	63.96	29.40	35.28	%
40000	13.21	20.42	20.87	21.93	23.37	23.92	18.23	N/mm²
%age difference	13.58	63.22	60.90	63.53	72.21	70.73	30.21	%
50000	15.85	25.40	23.51	24.57	25.11	25.47	20.17	N/mm²
%age difference	36.28	103.03	81.26	83.22	85.04	81.79	44.07	%
60000	16.39	27.57	26.83	27.61	27.23	25.93	22.53	N/mm²
%age difference	40.92	120.38	106.86	105.89	100.66	85.08	60.92	%

Table 4: Details of Tensile Strength of baked Clay as Percentage of Cube Crushing Strength

Load "N"	Pure Clay f_{cu} N/mm²	Pure Clay f_{bt} N/mm²	Pure Clay $\frac{f_{bt} \times 100}{f_{cu}}$	Pure Clay + 10% Pit-Sand f_{cu} N/mm²	Pure Clay + 10% Pit-Sand f_{bt} N/mm²	Pure Clay + 10% Pit-Sand $\frac{f_{bt} \times 100}{f_{cu}}$	Pure Clay + 20% Pit-Sand f_{cu} N/mm²	Pure Clay + 20% Pit-Sand f_{bt} N/mm²	Pure Clay + 20% Pit-Sand $\frac{f_{bt} \times 100}{f_{cu}}$	Pure Clay + 30% Pit-Sand f_{cu} N/mm²	Pure Clay + 30% Pit-Sand f_{bt} N/mm²	Pure Clay + 30% Pit-Sand $\frac{f_{bt} \times 100}{f_{cu}}$	Pure Clay + 40% Pit-Sand f_{cu} N/mm²	Pure Clay + 40% Pit-Sand f_{bt} N/mm²	Pure Clay + 40% Pit-Sand $\frac{f_{bt} \times 100}{f_{cu}}$	Pure Clay + 50% Pit-Sand f_{cu} N/mm²	Pure Clay + 50% Pit-Sand f_{bt} N/mm²	Pure Clay + 50% Pit-Sand $\frac{f_{bt} \times 100}{f_{cu}}$	Pure Clay + 60% Pit-Sand f_{cu} N/mm²	Pure Clay + 60% Pit-Sand f_{bt} N/mm²	Pure Clay + 60% Pit-Sand $\frac{f_{bt} \times 100}{f_{cu}}$
00	11.63	2.31	19.86	12.51	1.99	15.90	12.97	1.87	14.41	13.41	1.73	12.90	13.57	1.61	11.86	14.01	1.29	9.20	14.00	1.21	8.64
10000	11.83	2.57	21.72	12.72	2.03	15.95	13.27	1.94	14.61	13.37	1.83	13.68	14.11	1.68	11.90	15.57	1.37	8.79	15.11	1.33	8.80
20000	12.27	2.69	21.92	16.90	2.17	12.84	16.60	1.99	11.98	16.21	1.89	11.65	16.64	1.74	10.45	16.93	1.42	8.38	15.27	1.39	8.10
30000	12.46	2.83	22.71	18.17	2.23	12.29	18.94	2.08	10.98	18.40	1.97	10.70	22.25	1.79	8.04	18.13	1.49	8.21	18.94	1.44	7.60
40000	13.21	2.96	22.40	20.42	2.29	11.21	20.87	2.17	10.39	21.93	2.11	9.62	23.37	1.85	7.91	23.92	1.54	6.43	18.23	1.51	8.28
50000	15.85	3.07	19.36	25.40	2.35	9.25	23.51	2.22	9.44	24.57	2.17	8.83	25.11	1.91	7.60	25.47	1.61	6.32	20.17	1.54	7.63
60000	16.39	3.13	19.00	27.57	2.41	8.74	26.83	2.28	8.49	27.61	2.21	8.00	27.23	1.96	7.19	25.93	1.66	6.40	22.53	1.59	7.05
MEAN			20.99			12.31			11.47			10.76			9.27			8.67			8.01

4. ACKNOWLEDGEMENT

Experimental study, the details of which are presented in this paper was conducted in the structures Laboratory, Department of Civil Engineering, Quaid-e-Awam University of Engineering Science & Technology [QUEST], Nawabshah. The authors are thankful to lab: staff for their assistance to conduct this study.

5. CONCLUSIONS

From this study it is concluded that:

(1) A very pronounced increase of specific weight as well as specific gravity is achieved by applying compression as compacting force on clay specimens.

(2) The compacting force shows remarkable favorable effect on shrinkage co-efficient as well as.

(3) Limit should be imposed on ratio of pit-sand which in no case shall exceed 30 percent.

(4) The behaviour of baked clay specimens show that this material holds promise for successful making and using of pre-cast structural panels as alternative to cement concrete.

(5) Tensile strength ranges between 21% to 8% of cube crushing strength within the parameters of this study.

(6) A maximum cube crushing strength of 27.61 N/mm^2 (3950 psi) was observed as compared to 20 N/mm^2 (3000 psi) for common cement concrete which is higher by 38.05 Percent.

(7) From the trend it can be inferred that the strength is bound to improve with further increase of compacting force and the study may be extended further by incrementing compacting force by 1 N/mm^2 upto a limit when the curve showing rate of improvement becomes asymptotic.

(8) Tensile strength of baked clay decreases with the increase of pit-sand ratio but it increases with the increase of compacting force in real terms. However, in terms of percentage of cube crushing strength, it shows remarkable decrease.

REFERENCES

[1] Memon. M., Ansari. A.A. & Shaikh. A.M., "Preliminary Study of Structural Properties of Baked Clay", Mehran University Research Journal of Engineering & Technology, Vol. 18, No.3, July, 99, pp.161-166, Jamshoro.

[2] Astill. A. W. and Martin. L. H.," Singly Reinforced Concrete Beams", Elementary Structural Design in Concrete to CP 110, Edward Arnold (Publication) Ltd, 41 Bed Ford Square, London, WCIB 3DP, pp. 77-79, 1982.

[3] ACI Committee 318,"Building Code Requirements for Reinforced Concrete (ACI 318-71),"American Concrete Institute, Detroit, 1971, pp. 78.

[4] I.D. Karsan and J.O. Jirsa, "Behaviour of Concrete Under Compressive Loadings," Journal of Structural Division, ASCE, Vol. 95, ST12, Dec 1969, pp. 2543-2563.

[5] Morgan. W., "Elementary Reinforced Concrete Design", Moment of Resistance of Homogenious Beam of Rectangular cross-section; Design of Simply Reinforced Concrete Beams Containing "Economic" Amount of Steel. Chapter III, pp.56-69, London Edward Arnold (publisher) Ltd., 1999.

CONTENTS

VOLUME 7	NO: 2	JUL-DEC-2006